國 立 交 通 大 學

電子工程學系　電子研究所碩士班

碩 士 論 文

矽基片雙抗諧振反射光波導感測器之元件設計、製作與其特性量測

Design, Fabrication, and Characterization of Si-Based Sensors Based on Dual Antiresonant Reflecting Optical Waveguides

研 究 生 ：李承翰　　Cheng-Han Lee

指導教授 ：黃遠東 博士　Dr. Yang-Tung Huang

中華民國 一〇一年 七 月

矽基片雙抗諧振反射光波導感測器之元件設計、製作與其特性量測

Design, Fabrication, and Characterization of Si-Based Sensors Based on Dual Antiresonant Reflecting Optical Waveguides

研 究 生：李承翰　　Student: Cheng-Han Lee

指導教授：黃遠東 博士　　Advisor: Dr. Yang-Tung Huang

國立交通大學

電子工程學系　電子研究所碩士班

碩 士 論 文

A Thesis

Submitted to Department of Electronics Engineering & Institute of Electronics

College of Electrical and Computer Engineering

National Chiao Tung University

In Partial Fulfillment of the Requirements

For the Degree of Master

In

Electronics Engineering

July 2011

Hsinchu, Taiwan, Republic of China

中華民國一〇一年七月

矽基片雙抗諧振反射光波導感測器之元件設計、製作與其特性量測

研究生：李承翰　　指導教授：黃遠東 博士

國立交通大學

電子工程學系　電子研究所碩士班

摘 要

本研究探討創新結構雙抗諧振反射光波導(ARROW)感測器的設計、製造與特性量測。對於一個抗諧振反射光波導結構而言，光場藉由在包覆層之間的抗諧振反射與空氣-導光層界面的全反射，將光侷限於核心層。抗諧振反射光波導結構可將光導引在較低的折射率，並可靈活地設計核心層的折射率與大小使與單模光纖相容。對於雙抗諧振反射光波導而言，則可以藉由控制最大耦合效率來製作一個定向耦合器，或兩個分離的光波導。基於抗諧振反射光波導結構，沒有任何彎折結構的矽基感測器可以被實現。我們利用轉移矩陣法（TMM）與等效折射係數法（EIM）來分析與設計抗諧振反射光波導結構。然後，我們用波束傳輸方法（BPM）來模擬雙抗諧振反射光波導傳感器的傳播特性。我們製作元件並量測特性。測量結果顯示，沒有彎折結構的矽基感測器是可以被實現的。

Design, Fabrication, and Characterization of Si-Based Sensors Based on Dual Antiresonant Reflecting Optical Waveguides

Student: Cheng-Han Lee Advisor: Dr. Yang-Tung Huang

Department of Electronics Engineering and

Institute of Electronics

National Chiao Tung University

ABSTRACT

The design, fabrication, and characterization of novel Si-based sensors based on dual antiresonant reflecting optical waveguides (ARROWs) are proposed. For an ARROW structure, the light is confined within the core layer by antiresonant reflection in the cladding layers and by total internal reflection at the air-core interface. It can guide lightwaves in low-index cores on a high-index substrate, and the refractive index and size of the cores can be flexibly designed to be compatible with single-mode fibers. For dual ARROW, it can operate as a directional coupler or as two decoupled waveguides by controlling maximum coupling efficiency. Based on these structure, Si-based sensors based on dual ARROWs structure without any bending structure can be realized. The characteristics of dual ARROW structures were analyzed with the transfer matrix method (TMM) and the effective index method (EIM). Then, we used the beam propagation method (BPM) to simulate the propagation characteristics of the dual ARROW sensor. The devices were fabricated and characterized. Experimental results show that our Si-based sensors based on dual ARROW structure without any bending structure can be realized.

Acknowledgement

First of all my sincere thanks to the guidance of Prof. Yang-Tung Huang, his guidance makes me a glimpse of integrated optics field of esoteric, he made discussions from time to time with me and pointing me in the right direction, so that I benefited in recent years. The completion of this thesis should also thank the great assistance of National Nano Device Laboratories (NDL), and the support of Nano Facility Center (NFC).

Thank all genial seniors, classmates, underclassmen. In two years, I shared the life of the laboratory and discussion of works with my dear members of ioLab. You make my master's life colorful. Thanks to Jian-Hua Chen and Hsin-Feng Hsu seniors who patiently pointed out the lack of my research, especially, when I lost my direction. Thank to Rong-Rong Nian, I-Chung Tsai, Zheng-Wen Lin, Jun-Hong Liao, Jie-Ting Chen, Yu-Chung Su, Yen-Ting Lin, and Ya-Jhih Lin, you brought me a lot of happiness in two years. I wouldn't forget our funny and interesting activities and keep them in my deeply grateful heart.

Finally, I would like to take this literature to my beloved parents.

This work was partly supported by the National Science Council of the Republic of China under contract NSC 100-2220-E-009-009.

Contents

List of Figures

List of Tables

Chapter 1

Introduction

Integrated optical devices have been increasingly studied over a decade [1], especially in the last several years. There are many features that are widely applied to engineering, medicine, and optoelectronics integration such as power splitters, chemical and/ or biochemical sensors [2,3], and wavelength demultiplexers. However, the device miniatruization, mechanical stability, and fabrication tolerance are much concerned. The requirements can be achieved by using the standard semiconductor processing technique. They offer the possibility of multiple devices on a single chip and the prospect of integrating optical and electrical functions to form a smart system.

In contrast to conventional waveguides, ARROW utilizes anti-resonant reflection as the guiding mechanism instead of total internal reflection can perform low-loss single-mode propagation with a relatively large core size. For a dual ARROW structure including two parallel waveguides, the coupling characteristics have been investigated. The coupling efficiency strongly depends on the structure symmetry such that the directional coupler or Y-junction devices can be realized without any bending structure. Many of ARROW-based devices were investigated, such as power dividers [4-6], wavelength demultiplexers, and Mach-Zehnder interferometer sensors. Among various kinds of functional devices, integrated optical sensors of the Fabry-

Perot, Mach-Zehnder, and dual-slab waveguide types for chemical and biochemical sensing applications have been realized [7-10]. Our sensor based on a dual ARROW structure includes four regions: the input region, the coupling region, the decoupling region, and the output region. The input region was set to stabilize the input field. The coupling region operated as 3-dB coupler which split the input field to two equal fields and coupled into the decoupling region. The decoupling region acted as a sensing region, and the output region combines two fields and filters out those modes with a low excitation coefficient or a high propagation loss. Instead of dual output cores, the single output core performs crosstalk immunity and measurement convenience due to a relatively large core size to provide efficient coupling with a single-mode fiber.

The organization of this thesis is as follows. In Chapter 2, the analytic methods for integrated optical waveguides will be presented, which include the transfer matrix method (TMM) [11], the effective index method (EIM) [12], the eigenmode propagation analysis, and the beam propagation method (BPM) [13]. The transfer matrix method was used to solve the dispersion relation of a multilayered slab waveguide which was called the multilayer stack theory. The effective index method was used to deal with those complicated 3-D waveguide structure. To study the wave propagation in device, the eigenmode propagation analysis and the finite-difference beam propagation method were employed.

In Chapter 3, basic characteristics of ARROW and dual-ARROW are discussed in detail. To design a waveguide sensing device, the propagation loss as well as the effective single-mode condition are the main concern. The coupling behavior and the coupling efficiency control of dual ARROW devices are investigated.

In Chapter 4, the configuration of the Si-based sensor based on dual ARROW structures is presented. In the lateral y-direction, dual ARROW-type structures fulfilled by a series of the strips were used for constracting a compact sensor. To

attain a low propagation loss for the fundamental mode, all the widths of the strips w_h and the distances w_l between the strips except the core width w_g must satisfy the transverse antiresonance condition. Based on the theories of ARROW and dual ARROW structures, the sensor was designed and the BeamPROP software included in the commercial software package R-soft V. 5.1 was used to simulate the characteristics of our designed devices.

In Chapter 5, the fabrication processes of Si-based sensors based on dual ARROW structures, and related parameters of the fabrication processes are introduced. After all of the fabrication processes were accomplished, the measurement system at $\lambda = 0.6328$ μm was established. Measurement results of Si-based sensors based on dual ARROW structures are discussed in Chapter 6. In Chapter 7, the discussions and conclusions of our study are given.

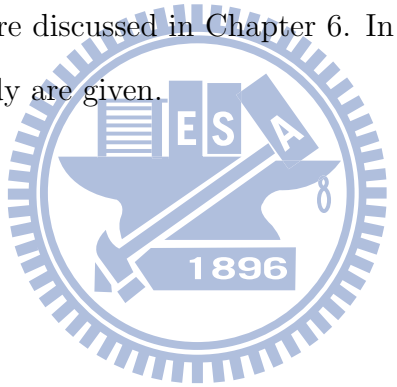

Chapter 2

Analytic Theories and Methods

Theories and Methods for the sensor based on dual antiresonant reflecting optical waveguides will be mentioned in this chapter. The sensor are based on multilayer structure. To realize lightwave characteristics such as propagation constant, dispersion relation, field distribution, and propagation loss, the transfer matrix method (TMM) [14] and normalization of guided modes are used. Additionally, For analyzing three-dimentional waveguide structures, we utilize the effective index method (EIM) [15] for handy analysis. To study the wave propagation in waveguides, the eigenmode propagation analysis and the finite-difference beam propagation method (FD-BPM) [16] are presented.

2.1 Transfer Matrix Method

The transfer matrix method is a numerical method for computing the electromagnetic modes supported by multilayer planar optical waveguides and can generate the dispersion relation governing the modes propagating in a multilayer slab waveguide and solve the real and imaginary parts of the propagation constants [17]. Basically, Maxwell's equations in a source-free, homogeneous, isotropic dielectric medium are expressed as

$$\vec{\nabla} \times \vec{E} = -j\omega\mu\vec{H}, \tag{2.1}$$

$$\vec{\nabla} \times \vec{H} = j\omega\epsilon\vec{E}. \tag{2.2}$$

Where $\omega = 2\pi c/\lambda_0$ is the angular frequency, c is the free-space light speed, and λ_0 is the wavelength. μ and ϵ are the magnetic permeability and the dielectric permittivity respectively. The electromagnetic fields of a plane wave propagating along the z-direction with the propagation constant β are in the form as

$$\vec{E} = E(x,y)e^{j(\omega t-\beta z)}, \tag{2.3}$$

$$\vec{H} = H(x,y)e^{j(\omega t-\beta z)}. \tag{2.4}$$

The multilayer slab waveguide is shown as Fig. (2.1), the electromagnetic fields are independent of y and the solutions of the wave equations can be classified into two types of modes with mutually orthogonal polarization states. In this case, we set $\partial E/\partial y = 0$ and $\partial H/\partial y = 0$, and substitute Eq. (2.3) and Eq. (2.4) into Eq. (2.1) and Eq. (2.2). One is the TE mode, which has zero longitudinal electric field ($E_z = 0$); the other is the TM mode, which has zero longitudinal magnetic field ($H_z = 0$). In the following, we will present the transfer matrix method [14] for the TE modes in a multilayer slab waveguide and the extension to TM modes by simple substitution rule will be given.

2.1.1 TE Modes

For TE modes in a slab structure, propagating along z-direction, which include field components H_x, E_y, and H_z. The relations between other components electromag-

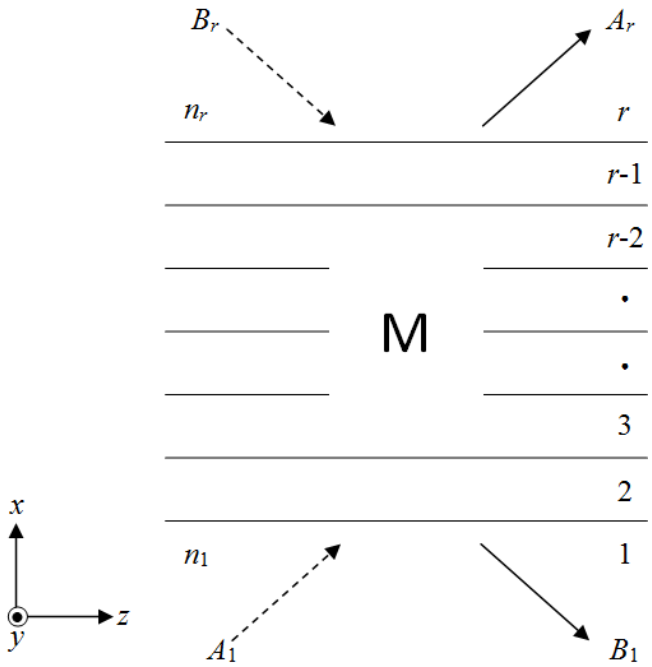

Figure 2.1: Sketch of a multilayer waveguide with the z propagation direction.

netic field in the Cartesian coordinate can be dissolved as

$$H_x = -\frac{\beta}{\omega\mu} E_y, \tag{2.5}$$

$$H_z = -\frac{1}{j\omega\mu} \frac{\partial E_y}{\partial x}, \tag{2.6}$$

$$E_y = -\frac{1}{j\omega\epsilon_0 n^2} \left(\frac{\partial H_z}{\partial x} + j\beta H_x \right), \tag{2.7}$$

$$E_x = E_z = H_y = 0, \tag{2.8}$$

here, we define two field varibles U and V by

$$U = E_y, \; V = \omega\mu H_z, \tag{2.9}$$

which describe the transverse electromagnetic field distributiion and are continuous at the layer boundaries. Then we substitute them into Eqs. 2.5-2.9 and obtain the relations

$$U' \equiv \frac{\partial U(x)}{\partial x} = -jV, \tag{2.10}$$

$$V' \equiv \frac{\partial V(x)}{\partial x} = j(\beta^2 - k^2 n^2)U, \tag{2.11}$$

where

$$k = \omega\sqrt{\mu_0\epsilon_0}, \tag{2.12}$$

$$n^2 = \frac{\epsilon}{\epsilon_0}, \tag{2.13}$$

while Eqs. 2.10 and 2.11 are differentiated with respect to x, it makes

$$U'' \equiv \frac{\partial^2 U(x)}{\partial x^2} = (\beta^2 - k^2 n^2)U, \tag{2.14}$$

$$V'' \equiv \frac{\partial^2 V(x)}{\partial x^2} = (\beta^2 - k^2 n^2)V, \tag{2.15}$$

The general solutions of Eq. (2.14) and (2.15) are

$$U = Ae^{-j\kappa x} + Be^{j\kappa x}, \tag{2.16}$$

$$V = j\frac{\partial U(x)}{\partial x} = \kappa(Ae^{-j\kappa x} - Be^{j\kappa x}), \tag{2.17}$$

where κ is the transverse propagation constant and

$$\kappa^2 = k^2 n^2 - \beta^2, \tag{2.18}$$

If bonudary conditions are set as $U_0 = U(0)$ and $V_0 = V(0)$ at the input plane $x = 0$ of the layer, i.e.,

$$U_0 = A + B,\ V_0 = \kappa(A - B), \tag{2.19}$$

we can get

$$A = \frac{1}{2}\left(U_0 + \frac{V_0}{\kappa}\right), \tag{2.20}$$

$$B = \frac{1}{2}\left(U_0 - \frac{V_0}{\kappa}\right), \tag{2.21}$$

A rearrangement of Eqs. 2.16-2.21 leads to a simple matrix $\mathbf{M}$ relation between the output quantities U, V and the input U_0, V_0

$$\begin{bmatrix} U_0 \\ V_0 \end{bmatrix} = \mathbf{M} \begin{bmatrix} U_0 \\ V_0 \end{bmatrix}, \tag{2.22}$$

where $\mathbf{M}$ is the "characteristic matrix" of the layer,

$$\mathbf{M} = \begin{bmatrix} \cos(\kappa x) & (j/\kappa)\sin(\kappa x) \\ j\kappa \sin(\kappa x) & \cos(\kappa x) \end{bmatrix}, \tag{2.23}$$

Next, consider a stack multilayer slab waveguide of r layers sandwiched between the substrate and cover, as shown in Fig. 2.1. The thickness and the refractive index of ith layer are d_i and n_i, where $i = 2 \sim r$-1. The characteristic matrix $\mathbf{M}$ at the ith layer is

$$\mathbf{M}_i = \begin{bmatrix} \cos(\kappa_i d_i) & (j/\kappa_i)\sin(\kappa_i d_i) \\ j\kappa_i \sin(\kappa_i d_i) & \cos(\kappa_i x_i) \end{bmatrix}, \tag{2.24}$$

where

$$\kappa_i^2 = k^2 n_i^2 - \beta^2, \tag{2.25}$$

The corresponding field variables of each layer are related by

$$\begin{bmatrix} U_{i-1} \\ V_{i-1} \end{bmatrix} = \mathbf{M}_i \begin{bmatrix} U_i \\ V_i \end{bmatrix}, \tag{2.26}$$

The input variables U_1, V_1 at the cover and the output variables U_r, V_r at the substrate, are related by

$$\begin{bmatrix} U_1 \\ V_1 \end{bmatrix} = \mathbf{M} \begin{bmatrix} U_r \\ V_r \end{bmatrix}, \tag{2.27}$$

where $\mathbf{M}$ is the characteristic matrix of the stack multilayer waveguide and the product of the individual matrices is given by

$$\mathbf{M} \equiv \begin{bmatrix} m_{11} & m_{12} \\ m_{21} & m_{22} \end{bmatrix} = \prod_{i=2}^{r-1} M_i = M_2\, M_3 \cdots M_{r-1}, \tag{2.28}$$

where m_{11}, m_{12}, m_{21}, and m_{22} are the matrix elements which will be used below. Since there is no wave in the cover along x-direction ($B_r = 0$) and in the substrate along $+x$-direction ($A_1 = 0$). The field variables in the top and bottom layer are given by

$$\begin{aligned} U_1 &= B_1,\ V_1 = -\kappa_1 B_1, \\ U_r &= A_r,\ V_r = \kappa_r A_r, \end{aligned} \tag{2.29}$$

Substituting Eq. (2.29) into Eq. (2.27), we can obtain the dispersion relation of multilayer slab waveguides as

$$\kappa_1(m_{11} + \kappa_r m_{12}) + (m_{21} + \kappa_r m_{22}) = 0 \tag{2.30}$$

Solving the dispersion relation, Eq. (2.30), we can obtain the propagation constants of TE modes for a multilayer slab waveguide.

2.1.2 TM Modes

For TM modes whose z-component magnetic field $H_z = 0$ propagating along z-direction, it can be derived that $H_x = E_y = 0$. According to Maxwell's equations, we can obtain the relations like that we derive for TE modes as

$$E_x = \frac{\beta}{\omega\epsilon_0 n^2} H_y, \tag{2.31}$$

$$E_z = \frac{1}{j\omega\epsilon_0 n^2} \frac{\partial H_y}{\partial x}, \tag{2.32}$$

$$H_y = \frac{1}{j\omega\mu} \left(\frac{\partial E_z}{\partial x} + j\beta E_x \right), \tag{2.33}$$

We can define two field variables U and V as

$$U = H_y,\ V = \omega\epsilon_0 E_z, \tag{2.34}$$

Substituting them into Eqs. 2.31-2.33, we obtain the relations

$$U' \equiv \frac{\partial U(x)}{\partial x} = jn^2 V, \tag{2.35}$$

$$V' \equiv \frac{\partial V(x)}{\partial x} = -j(\frac{\beta^2}{n^2} - k^2)U, \tag{2.36}$$

Differentiating Eqs. 2.35 and 2.36 with respect to x, we can obtain

$$U'' \equiv \frac{\partial^2 U(x)}{\partial x^2} = (\beta^2 - k^2 n^2)U, \tag{2.37}$$

$$V'' \equiv \frac{\partial^2 V(x)}{\partial x^2} = (\beta^2 - k^2 n^2)V, \tag{2.38}$$

The general solutions of Eqs. 2.37 and 2.38 are

$$U = Ae^{-j\kappa x} + Be^{j\kappa x}, \tag{2.39}$$

$$V = \frac{1}{jn^2}\frac{\partial U(x)}{\partial x} = -\frac{\kappa}{n^2}(Ae^{-j\kappa x} - Be^{j\kappa x}), \tag{2.40}$$

where

$$\kappa^2 = k^2n^2 - \beta^2, \tag{2.41}$$

Similarly, we can get the transfer matrix of the TM modes as

$$\mathbf{M}_i = \begin{bmatrix} \cos(\kappa_i d_i) & -j(\frac{n_i^2}{\kappa_i})\sin(\kappa_i d_i) \\ -j\frac{\kappa_i}{n_i^2}\sin(\kappa_i d_i) & \cos(\kappa_i d_i) \end{bmatrix}, \tag{2.42}$$

and the dispersion relation of TM modes is then given by

$$\frac{\kappa_1}{n_1^2}(m_{11} + \frac{\kappa_r}{n_r^2}m_{12}) + (m_{21} + \frac{\kappa_r}{n_r^2}m_{22}) = 0 \tag{2.43}$$

We can get the propagation constants of the TM modes by solbing the dispersion relation, Eq. (2.43).

2.2 Effective Index Methods

The effective index method (EIM) was initially proposed from modifying Marcatili's method [18] for the analysis of rectangular-core dielectric waveguides [19]. The effective index method is an approximate calculation in dealing with complicated 3-D waveguide structure and the basic principle is to replace the waveguide by an equivalent slab waveguide with a refrative index profile from the geometrical shape of the original waveguide. The effective index might be the most popular one of several approximate techniques because of this method makes the analysis more efficient and simpler.

As shown in Fig. 2.2 the ridge 3-D structure is divided into 2-D waveguide with light confinement in the lateral y-direction. The 3-D structure is divided into

three regions. In each region, the transfer matrix method is applied to solve the effective index in the vertical x-direction. We can use the transfer matrix again and obtain the final effective index in the lateral y-direction with index distribution of $N'_{\text{eff}}/N_{\text{eff}}/N'_{\text{eff}}$.

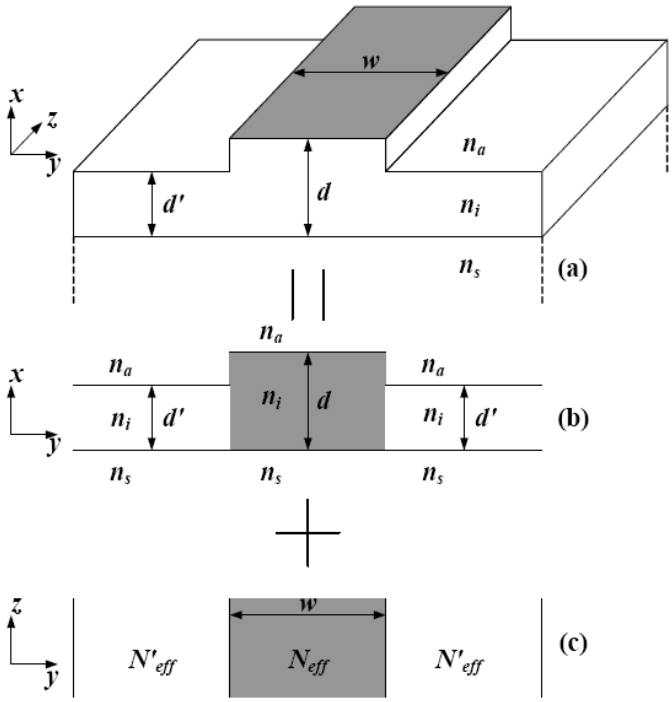

Figure 2.2: Effective Index Method: (a) 3-D ridge waveguide; (b) 2-D equivalence in the x-y plane; (c) 2-D equivalence in the y-z plane.

2.3 Eigenmode Propagation Analysis

Assume that a light wave is launched into a waveguide at $z = 0$. The input field profile $\Psi(x, 0)$ can be expanded in terms of all eigenmodes:

$$\Psi(x, 0) = \sum_{\nu} c_\nu \psi_\nu(x), \tag{2.44}$$

where the summation takes account of guided and radiation modes, and $\psi_\nu(x)$ is the normalized modal field distribution of mode ν. The field excitation coefficient

c_ν can be found by calculating overlap integrals as

$$c_\nu = \frac{\int \Psi(x)\psi_\nu(x)\mathrm{d}x}{\int \psi_\nu^*(x)\psi_\nu(x)\mathrm{d}x}, \tag{2.45}$$

and the square of its absolute value $|c_\nu|^2$, the excitation efficiency, represents the power ratio carried by the mode. The field profile at a distance z can then be expressed as the superposition of all eigenfunctions:

$$\Psi(x,z) = \sum_\nu c_\nu \psi_\nu(x) \cdot \exp(-j\beta_\nu z), \tag{2.46}$$

where β_ν is the propagation constant of mode ν. For the analysis of leaky waveguides such as ARROW structures, the eigenmode expansion and normalization based on leaky mode approximations can be applied [20].

2.4 Beam Propagation Method

The beam propagation method (BPM), is a numerical method to analyze light propagation phenomena in the waveguide by solving scalar wave equation along the longitudinal direction of the waveguide. BPM derives from a paraxial form of the Helmholtz equation, known as the Fresnel equation, is valid for paraxial propagation in slowly varying optical waveguide. This method is in common use on waveguide structures with arbtrary cross-section geometries.

In most cases, it is possible to treat the optical propagation problem starting from the salar Helmholtz equation. The three-dimension scalar wave equation is expressed by

$$\frac{\partial^2 E}{\partial x^2} + \frac{\partial^2 E}{\partial y^2} + \frac{\partial^2 E}{\partial Z^2} + k_0^2 n^2(x,y,z)E = 0, \tag{2.47}$$

where E is the electric field and n is the refractive index in the domain of interest. We assume that the field $E = \psi(x,y,z)\exp^{-jk_0 n_0 z}$, where ψ is an axially slowly varying function, n_0 is the mean refractive index of the medium and z is the propagation

direction. For a light beam confined in a two-dimensional cross-sectional waveguide with an index profile $n(x,z)$ and paraxial propagating along the z-direction, the scalar wave equation can be described as

$$\frac{\partial^2\Psi}{\partial x^2} + \frac{\partial^2\Psi}{\partial z^2} + k_0^2 n^2(x,z)\Psi = 0, \tag{2.48}$$

Assume $\Psi = \psi(x,z)\exp(-jk_0n_0z)$ is a wave propagating mainly in the z-direction. With the slowly varying envelope approximation [36,37], Eq. (2.48) can be reduced to

$$2jk_0n_0\frac{\partial\psi}{\partial z} = \frac{\partial^2}{\partial x^2}\psi + k_0^2[n^2(x,z) - n_0^2]\psi, \tag{2.49}$$

Then we use a uniform discretization step sizes Δx and Δz. So we find

$$2jk_0n_0\frac{\partial\psi_i}{\partial z} = \frac{\psi_{i+1} + \psi_{i-1} - 2\psi_i}{(\Delta x)^2} + k_0^2[n^2(x,z) - n_0^2]\psi_i, \tag{2.50}$$

where ψ_i is the field at $(u\Delta x, z)$and Δx denotes the discretization step in the x-direction. This process can be repeated until the wave reaches the boundary of the domain resulting in final field distribution. The finite difference BPM (FDBPM) is more accurate than conventional fast Fourier transform (FFTBPM) in high index contrasts.

There is another method, called Crank-Nicolson scheme, a linear combination of the "forward-diffrence" method and the "backward-diffrence" method. Applying the Crank-Nicolson scheme, we obtain

$$\psi_{i-1}^{\nu+1} + a_i^+\psi_i^{\nu+1} + \psi_{i+1}^{\nu+1} = -\psi_{i-1}^{\nu} - a_i^-\psi_i^{\nu} - \psi_{i+1}^{\nu}, \tag{2.51}$$

where

$$a_i^+ = -2 + k_0^2(n_i^2 - n_0^2)(\Delta x)^2 - 4jk_0n_0(\Delta x)^2/\Delta z, \tag{2.52}$$

$$a_i^- = -2 + k_0^2(n_i^2 - n_0^2)(\Delta x)^2 + 4jk_0n_0(\Delta x)^2/\Delta z, \tag{2.53}$$

The superscripts and subscripts in Eq. (2.51) denote the z- and x-coordinates, respectively. For example, ψ_i^{nu} is the slowly-varying field at $(\mathrm{i}\cdot\Delta x, \nu\cdot\Delta z)$.

To deal with the radiation reflected back from the computation boundaries, the transparent boundary condition (TBC) [21] is used. For waveguide structures whose refractive indices differ greatly from the average refractive index (the reference index), the Padé approximant operator [22] is also implemented in the simulation. For this reseach here, we use the BeamPROP software included in the commerical software package R-soft V. 5.1 to simulate the characteristics of our designed devices.

Chapter 3

Dual Antiresonant Reflecting Optical Waveguide (ARROW)

3.1 Introduction

ARROW structure utilizes the Fabry-Perot reflection [23] instead of the total internal reflection (TIR) as the guiding mechanism. With antiresonant reflection, the core size can be less constrained to increase its thickness. Thus, it is suitable for efficient connection to fibers. The relationship of propagation loss was shown as Eq. (3.1) [24]

$$\alpha_\nu \lambda \propto \frac{(\nu+1)^{2L+2}}{4^L d^{2L+3}}, \tag{3.1}$$

Where ν is the ν th mode, L is cavity pair number, and d is core thickness. From this relationship, we can obtain a low-loss and single-mode propagation by controlling these parameters.

Antiresonant reflection makes constructive interference in core layer and destructive interference in cladding layers to confine the lightwaves. In contrast to conventional waveguides, the coupling length of ARROW-based couplers does not increase but varies as a periodic function of waveguide separation such that remote coupling can be realized [25]. Based on this structure, Moreover, the ARROW structure can be developed to 3-dB coupler-like device. In a dual ARROW structure, the coupling

efficiency C(z) from one waveguide core to the other at any position z can be defined as the ratio of the power transferred $\triangle P_2(z)$ to the initial power $P_1(0)$, and can be expressed as Eq. (3.2) [22]

$$C(z) \equiv \frac{\triangle P_2(z)}{P_1(0)} = C_0 \sin\left(\frac{\beta_e - \beta_o}{2} z\right), \tag{3.2}$$

Where P_1 and P_2 are the guided powers in the upper and lower cores, and β_e and β_o are the propagation constants of the fundamental even and odd modes, respectively. C_0 represents the maximum coupling efficiency at the coupling length which is shown in Eq. (3.3).

$$L_0 = \frac{\lambda}{2|N_e - N_o|}, \tag{3.3}$$

Where λ is the operation wavelength of 0.6328 μm and N_e, N_o are the real part of effective indices of even and odd modes, respectively.

The coupling efficiency strongly depends on the structure symmetry. The higher symmetry degree is, the higher coupling efficiency is, and vice versa. The simulation shows coupling efficiency can be controlled from near 100% to 0%. According to these advantages, we can design the ARROW structure along lateral direction to compatible with a single-mode fiber. Moreover, it can construct many applications such as uncoupled stack configurations, wavelength demultiplexers and filters, polarization splitters, and power dividers for optical interconnections, communications, signal processing, and sensing.

3.2 Characteristics of an ARROW Structure

The basic structure of ARROW is shown in Fig. 3.1. The refractive index in this structure is arranged in order of $n_{\mathrm{a}}/n_{\mathrm{g}}/n_{\mathrm{h}}/n_{\mathrm{l}}/n_{\mathrm{s}}$. Considering refractive index of core, first cladding, and second cladding, the relative value is low, high, and low, respectively. In contrast to conventional waveguides, ARROW structure utilizing antiresonant reflection as a guiding mechanism instead of total internal reflection

can guide waves in low-index cores on a high-index substrate. The schematic view is shown in Fig. 3.2. By this structure, the low-loss single-mode propagation with a relatively large core size can be achieved. To summary features of ARROW structure: (a) effective single-mode propagation, (b) low loss of effective single mode, (c) large core size suitable for efficient connections to single mode fibers, (d) various choice of waveguide materials for each layer, (e) flexible fabrication tolerance and design rule.

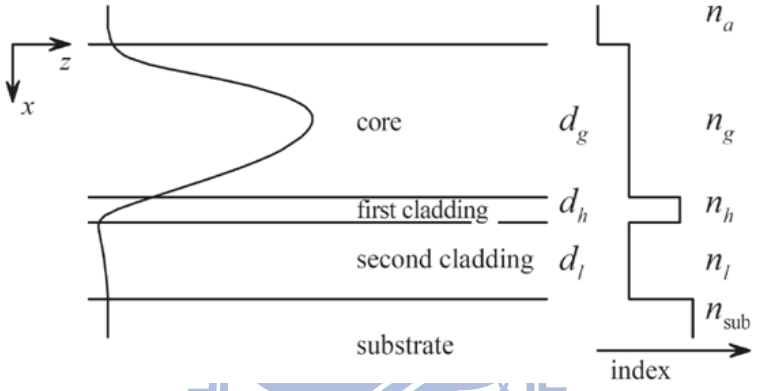

Figure 3.1: The cross-section schematic of a slab ARROW waveguide.

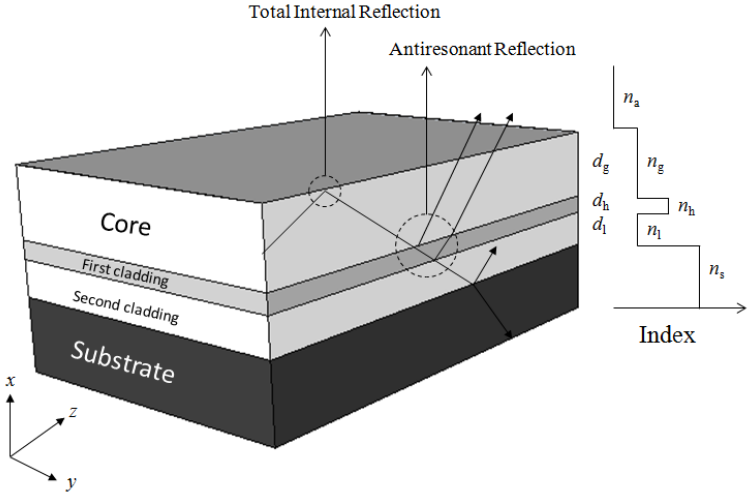

Figure 3.2: Light propagation behavior and the refractive indices of the core and the cladding layers in a ARROW structure.

Following description, we derive the confinement condition of the planar AR-

ROW structure from the ray-optical picture, as shown in Fig. 3.2. We supposed the zig-zag beam with a certain incident angle is guided in the core region. The optical field decays evanescently in the air region because of the total internal reflection at the air-core interface. The transverse propagation constant κ_{g} in the core region and κ_{a} in the air region are given by

$$\kappa_g = \sqrt{k_0^2 n_g^2 - \beta^2}, \tag{3.4}$$

$$\kappa_a = -j\gamma_a, \tag{3.5}$$

$$\gamma_a \equiv \sqrt{\beta^2 - k_0^2 n_a^2}, \tag{3.6}$$

where $k_0 n_{\mathrm{g}} > \beta > k_0 n_{\mathrm{a}}$, and β is the propagation constant.

For TE mode, the reflection coefficient γ_{ga} at the air-core interface is given by

$$\gamma_{\mathrm{ga}} \equiv \frac{\kappa_{\mathrm{g}} - \kappa_{\mathrm{a}}}{\kappa_{\mathrm{g}} + \kappa_{\mathrm{a}}} = \frac{\kappa_{\mathrm{g}} + j\gamma_{\mathrm{a}}}{\kappa_{\mathrm{g}} - j\gamma_{\mathrm{a}}} \equiv \mid \gamma_{\mathrm{gh}} \exp(j\phi_{\mathrm{gh}}) \mid, \tag{3.7}$$

where $\kappa_{\mathrm{h}} \gg \kappa_{\mathrm{g}}$, so ϕ_{gh} approaches π.

In order to form a constructive interference in the core layer, the following condition should be satisfied

$$-2\kappa_{\mathrm{g}} d_{\mathrm{g}} + \phi_{\mathrm{ga}} + \phi_{\mathrm{gh}} = 0 \Rightarrow \kappa_{\mathrm{g}} d_{\mathrm{g}} \approx \pi, \tag{3.8}$$

if the core size is not large enough, Eq. (3.8) must be modified as

$$2\kappa_{\mathrm{g}} d_{\mathrm{ge}} = 2\pi \Rightarrow \kappa_{\mathrm{g}} d_{\mathrm{ge}} = \pi, \tag{3.9}$$

where d_{ge} is the effective thickness of the core layer.

Rearranging Eq. (3.8) and applying Snells law, we can derive Eq. (3.10) as

$$\begin{aligned} & \frac{2\pi}{\lambda} n_{\mathrm{g}} \cos\theta_{\mathrm{g}} d_{\mathrm{g}} \approx \pi, \\ \Rightarrow \quad & \cos\theta_{\mathrm{h}} = (1 - \sin^2\theta_{\mathrm{h}})^{\frac{1}{2}} \\ = \quad & \left(1 - \frac{n_{\mathrm{g}}^2}{n_{\mathrm{h}}^2}\sin^2\theta_{\mathrm{g}}\right)^{\frac{1}{2}} \approx \left(1 - \frac{n_{\mathrm{g}}^2}{n_{\mathrm{h}}^2} + \frac{\lambda_0^2}{4n_l^2 d_{\mathrm{g}}^2}\right)^{\frac{1}{2}}, \end{aligned} \tag{3.10}$$

where θ_g and θ_h respectively represent the ray angle in the core layer and the first cladding layer. From the transmission characteristics of a Fabry-Perot resonator, high reflection of cladding layer exists under the antiresonance condition. The antiresonance condition is defined as

$$2\kappa_i d_i = (2m+1)\pi, m = 0, 1, 2, ..., \tag{3.11}$$

where Eqs. 3.10 and 3.11, the antiresonance conditions of the first and the second cladding layers are derived as

$$d_{\mathrm{h}} = \frac{\lambda}{4n_{\mathrm{h}}}\left(1 - \frac{n_{\mathrm{g}}^2}{n_{\mathrm{h}}^2} + \frac{\lambda_0^2}{4n_h^2 d_{g^2}}\right)^{-\frac{1}{2}}(2P+1), P = 0, 1, 2, ..., \tag{3.12}$$

$$d_{\mathrm{l}} = \frac{\lambda}{4n_{\mathrm{l}}}\left(1 - \frac{n_{\mathrm{g}}^2}{n_l^2} + \frac{\lambda_0^2}{4n_{\mathrm{l}}^2 d_{\mathrm{g}^2}}\right)^{\frac{1}{2}}(2Q+1), Q = 0, 1, 2, ..., \tag{3.13}$$

If the refractive index of the second cladding layer n_l and the core layer n_g are the same, Eq. (3.13) can be simplified as

$$d_{\mathrm{l}} \approx \frac{d_g}{2}(2Q+1). \tag{3.14}$$

3.3 Characteristics of Dual ARROW Structure

Coupling between two parallel waveguides has been widely investigated [26]-[31]. The coupling behavior was proposed by Baba et. al. for using as an uncoupled stacking [32]. Their results are shown only in weakly coupling situation, and dual-ARROW structures with leaky modes, the strong coupling between two waveguides must be considered. The underlying principle behind these distinct phenomena has been successfully revealed [23], and it is found that a dual ARROW can operate as a directional coupler or as two decoupled waveguides by controlling the structural symmetry. In the following , the coupling efficiency analysis of dual ARROW structures is briefly summarized. In the analysis, we employ the method based on

interference of the even and odd lowest order modes to analyze the coupling efficiency of a dual-ARROW structure [33]. Although there might exist some other higher order modes with low propagation loss, only these two lowest order modes can be efficiently excited. The field distributed in a dual ARROW guided system can be expressed as

$$E(x,z) = A_{\mathrm{e}}E_{\mathrm{e}}(x)\exp(-jk_0N_{\mathrm{e}}z) + A_{\mathrm{o}}E_{\mathrm{o}}(x)\exp(-jk_0N_0z), \tag{3.15}$$

$$H(x,z) = A_{\mathrm{e}}H_{\mathrm{e}}(x)\exp(-jk_0N_{\mathrm{e}}z) + A_{\mathrm{o}}H_{\mathrm{o}}(x)\exp(-jk_0N_0z), \tag{3.16}$$

where A_{e} and A_{o} are amplitudes of the normalized even and odd modes with effective indices N_{e} and N_{o}, respectively. Both E_{e} (H_{e}) and E_{o} (H_{o}) are the normalized electric (magnetic) fields of even and odd modes, respectively. For TE modes, the power density S_z is

$$\begin{aligned} S_z(x,z) &= \frac{1}{2}\mathrm{Re}\left[\left(\overrightarrow{E}\times\overrightarrow{H}^*\right)\cdot\widehat{a}_z\right] = \frac{1}{2}\mathrm{Re}\left[E_y(x,z)H_x^*(x,z)\right] \\ &= \frac{1}{2}\mathrm{Re}[A_{\mathrm{e}}^2E_{\mathrm{e}}(x)H_{\mathrm{e}}^*(x) + A_{\mathrm{o}}^2E_{\mathrm{o}}(x)H_{\mathrm{o}}^*(x)y \\ &\quad + A_{\mathrm{e}}A_{\mathrm{o}}\cdot[E_{\mathrm{e}}(x)H_{\mathrm{o}}^*(x) + E_{\mathrm{o}}(x)H_{\mathrm{e}}^*(x)]\cdot\cos\left[k_0\left(N_{\mathrm{e}}-N_{\mathrm{o}}\right)z\right]], \end{aligned} \tag{3.17}$$

The even and odd modes are orthonormal with respect to the Poynting power as

$$P = \int_{-\infty}^{\infty} S_z(x,z)\mathrm{d}x = P_{\mathrm{g1}} + P_{\mathrm{g2}} + P_{\mathrm{else}} = \left(A_{\mathrm{e}}^2 + A_{\mathrm{o}}^2\right) = 1, \tag{3.18}$$

where

$$P_{\mathrm{g1}}(z) = \int_{\mathrm{g1}} S_z(x,z)\mathrm{d}x, P_{\mathrm{g2}}(z) = \int_{\mathrm{g2}} S_z(x,z)\mathrm{d}x, \text{ and } P_{\mathrm{else}}(z) = \int_{\mathrm{else}} S_z(x,z)\mathrm{d}x. \tag{3.19}$$

P_{g1} is the guided power in the first core, P_{g2} is the guided power in the second core, and P_{else} represents the remaining power in the region outside first core and second core.

Light is launched to the first core g_1 in Fig. 3.3 at the reference plane $z = 0$ such that there is a reference power P_{g1} guided in the first core.

To calculate the coupling efficiency $C(z)$ from the first core in our structure to the second core at any z position, we must investigate the power variation $\triangle P_{g2}$ in the second core. The power in the first core at a position z is

$$P_{g1}(z) = A_e^2\xi_{ee} + A_e^2\xi_{oo} + A_eA_o(\xi_{eo} + \xi_{oe})\cos[k_0(N_e - N_o)z], \tag{3.20}$$

where

$$\xi_{ij} = \frac{1}{2}\int_{g1} E_j(x)H_i^*(x)\mathrm{d}x, \ (i, j = e, o). \tag{3.21}$$

To minimize the uncoupled power $P_{g2}(0)+P_{else}(0)$, the cross product A_eA_o is obtained as

$$A_eA_o = \frac{\xi_{eo} + \xi_{oe}}{\left[(\xi_{ee} - \xi_{oo})^2 + (\xi_{eo} + \xi_{oe})^2\right]^{\frac{1}{2}}} \tag{3.22}$$

Assume that the power is mainly guided inside g_1 and g_2, then

$$\triangle P_{else}(z) \ll \triangle P_{g2}(z), \tag{3.23}$$

and we can utilize the following approximatiions:

$$\begin{aligned} \triangle P_{g2}(z) &\approx -\triangle P_{g1}(z) = P_{g1}(0) - P_{g1}(z) \\ &= 2A_eA_o(\xi_{eo} + \xi_{oe})\sin^2\left[\frac{k_0(N_e - N_o)}{2}z\right]. \end{aligned} \tag{3.24}$$

Based on above equations, we obtain the coupling efficiency as

$$C_0 = \frac{2(\xi_{eo} + \xi_{oe})^2}{(\xi_{ee} + \xi_{oo})\left[(\xi_{ee} - \xi_{oo})^2 + (\xi_{eo} - \xi_{eo})^2\right]^{\frac{1}{2}} + \xi_{ee} - \xi_{oo})^2 + (\xi_{eo} - \xi_{eo})^2}, \tag{3.25}$$

$$\beta_c = \frac{k_0(N_e - N_o)}{2}, \tag{3.26}$$

and C_0 represents the maximum coupling efficiency at a length z equal to the coupling length (L_c). In the case that light is launched to the second ARROW waveguide, the above formulas will also be satisfied if P_{g1} and P_{g2} are exchanged with each other.

The size is one of the most important factors in the cost and integration capability for an integrated opticcal device and a compact device is always attractive, it is desirable to shorten the coupling length and in turn the device length for a coupler. We design our devices by using this theory.

3.4 Coupling Behavior of Dual ARROW Structures

The basic configuration of dual ARROW structure is shown in Fig. 3.3 which consists of two cores, a separation layer, and five sets of antiresonant cavities neighboring on core layer. The structure of the refractive index is arranged in order of $(n_{\rm l}/n_{\rm h})_5/n_{\rm g1}/n_{\rm h}/n_{\rm sep}/n_{\rm h}/n_{\rm g2}/(n_{\rm h}/n_{\rm l})_5$. Two core layers are with the low refractive indices of n_{g1} and n_{g2} which are the same to sencond cladding, and the thicknesses are $d_{\rm g1}$ and $d_{\rm g2}$, respectively. Between the two cores is a three-layered structure with a high-low-high index profile $n_{\rm h}/n_{\rm sep}/n_{\rm h}$ and corresponding thicknesses are $d_{\rm h}/d_{\rm sep}/d_{\rm h}$. Atop the first core are with indices $n_{\rm l}/n_{\rm h}$ and thicknesses $d_{\rm l}/d_{\rm h}$. Opposite side (below the second core) are with refractive indices $n_{\rm h}/n_{\rm l}$ and its thicknesses are $d_{\rm h}/d_{\rm l}$. In order to obtain highest symmetry, the refractive indices and thicknesses of the core layers are set to be the same, i.e., $n_{\rm g1} = n_{\rm g2}$ and $d_{\rm g1} = d_{\rm g2}$. Except the separation layer, all cladding layers satisfy the antiresonance condition. As the coupling strength between dual ARROW waveguides strongly depends on the degree of their symmetry, we can adjust the reflective index of the second core layer to spoil structural symmetry to change the coupling efficiency.

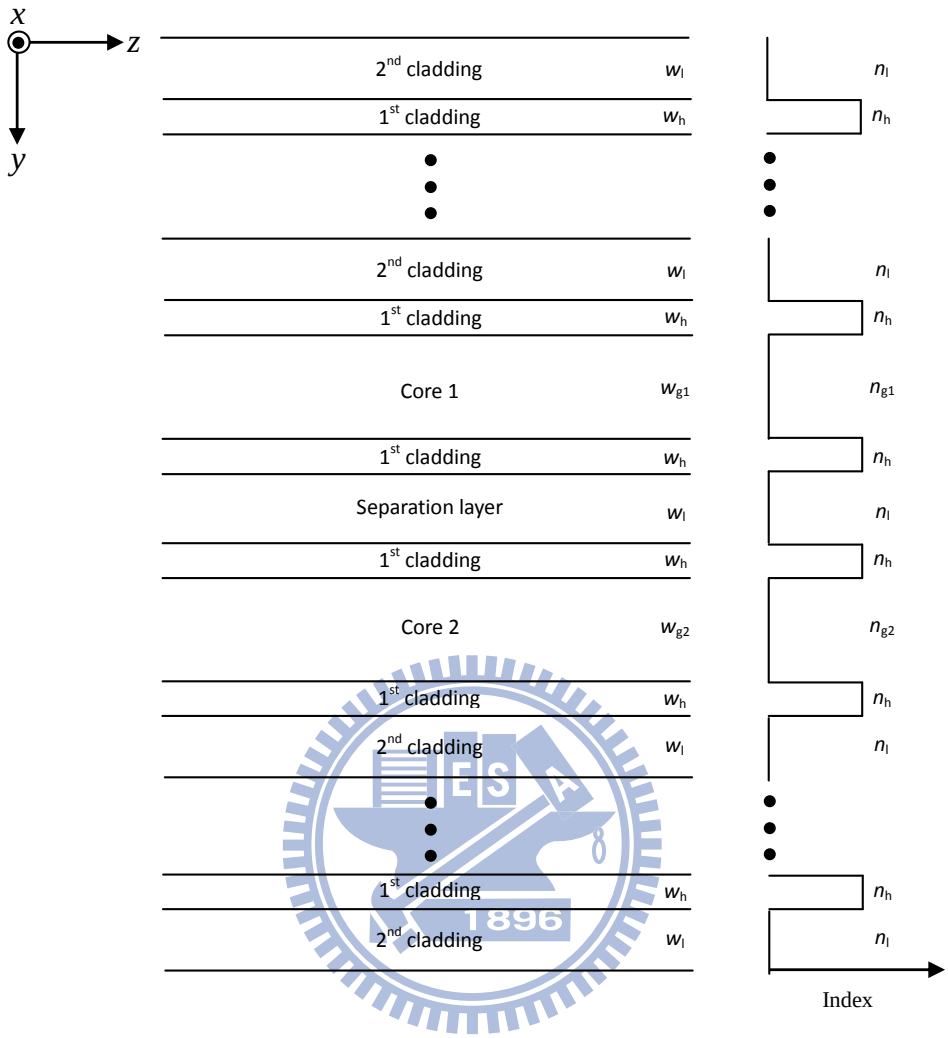

Figure 3.3: The schematic view of a dual ARROW waveguide.

Figure 3.4 shows the dependence of the maximum coupling efficiency on the refractive index of the second core layer n_{g2}. It can be seen that an efficient coupling occurs when the structure reach the relatively high symmetry ($n_{g2} \simeq 1.773$ RIU) and the maximum coupling efficiency is close to 100%. When the refractive index of the second core layer is lightly changed, the maximum coupling efficiency is dropped to less than 2%.

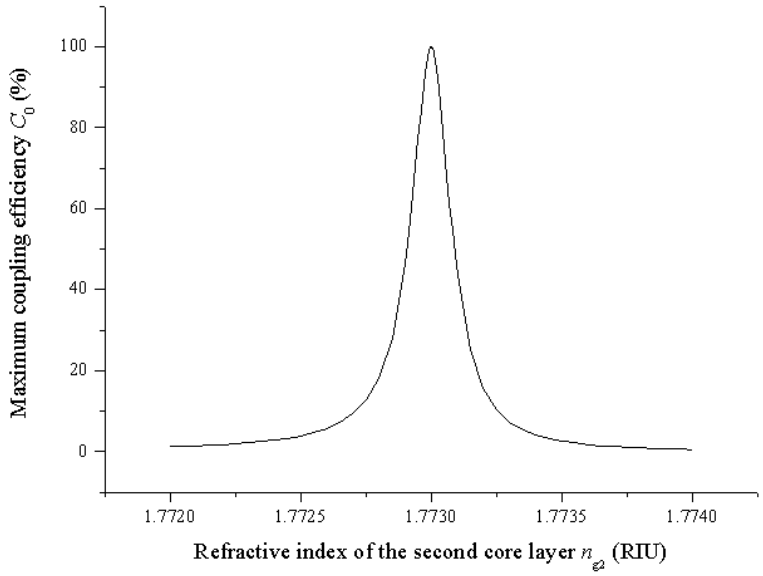

Figure 3.4: Maximum coupling efficiency as a function of the refractive index of the second core layer. The parameters are: $n_{g1} = n_{g2} = n_l = 1.773$ RIU, $n_h = 1.817$, $d_{g1} = d_{g2} = 4$ μm, $d_h = 0.39$ μm, and $d_l = 2$ μm.

3.5 Summary

In this chapter, the features of ARROW and dual ARROW structure are investigated. Based on these characteristics, we can control the coupling efficiency between near 0% and 100% by adjusting the symmetric degree of the horizontal structure. Therefor, we can construct the power splitter without any bending structure by the combination of coupling and decoupling regions. In addition to techniques which can be used to shorten the length of an ARROW-based coupler, a critical design consideration for 3-dB couplers is also presented.

Chapter 4

Design and Simulation Results of the Si-Based Sensor based on Dual ARROW Structures

4.1 Design of the Slab Waveguide Structure

Figure 4.1 shows the schematic view of the Si-based sensor based on dual ARROW structures. The top and cross-sectional views are shown in Fig. 4.2. In the slab structure, we chose silicon oxide as the capping layer and the lower cladding layer, and silicon nitride as the core layer. Refractive indices of the capping layer n_{p}, the core layer n_{c}, and the lower cladding layer n_{b} are chosen as 1.46, 2.00, and 1.46, respectively. The thickness of the core layer (d_{c}) was designed as 0.18 μm which was calculated by cutoff condition for single-mode propagation. Then we designed the thicknesses of the capping layer (d_{p}) and lower cladding layer (d_{b}) as 0.8 μm and 1 μm, respectively. Our fabrication process was chosen (100) p-type silicon as the substrate. The parameters of the slab waveguide are shown in Table 4.1, and the operation wavelength λ is 0.6328 μm.

In the vertical direction, the structure was designed as the conventional waveguide. Based on cutoff condition, the lightwave in the core layer can provide single mode propagation. In the lateral direction, the lightwave was confined by ARROW

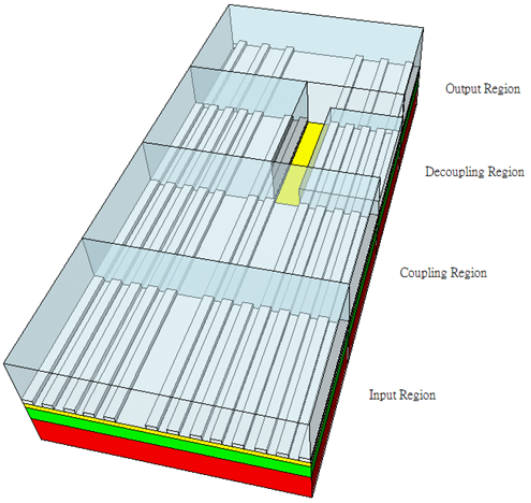

Figure 4.1: The schematic view of the Si-based sensor based on dual ARROW structures

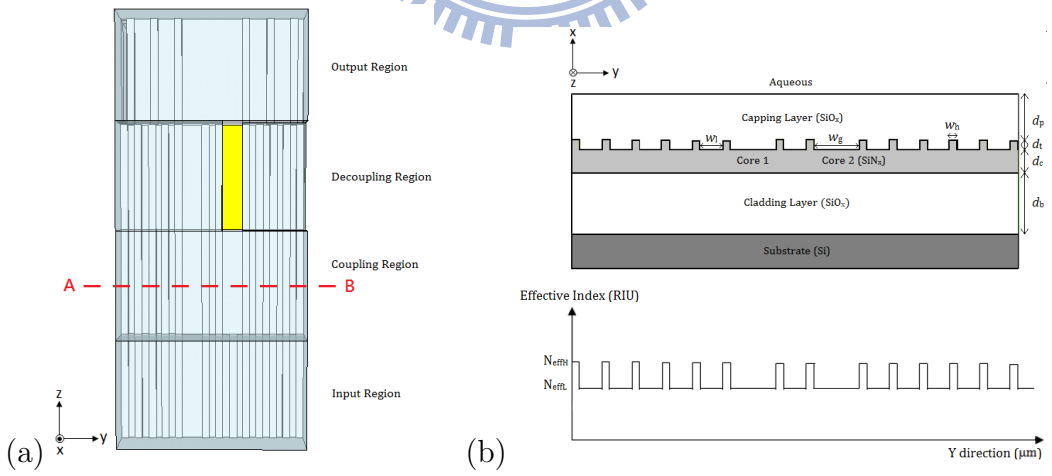

Figure 4.2: (a) The top view of the Si-based sensor based on dual ARROW structures, (b) The cross-sectional view and the corresponding effective index of the slab waveguide structure across the A-B line.

Table 4.1: The parameters of the slab waveguide structure at the operation wavelength λ of 0.6328 μm.

Layer	Material	Refractive Index (RIU)	Thickness (μm)
Superstrate	H_2O	$n_a = 1.332$	$d_a = 30$ μm
Capping layer	SiO_x	$n_p = 1.46$	$d_p = 0.80$ μm
Nitride strip	SiN_x	$n_t = 2.00$	$d_t = 0.04$ μm
Core layer	SiN_x	$n_c = 2.00$	$d_c = 0.18$ μm
Lower cladding layer	SiO_x	$n_b = 1.46$	$d_b = 1.00$ μm
Substrate	Si-wafer	$n_s = 3.85$	$d_s = 30.00$ μm

structures with the expansion of cavities which conform to antiresonant condition in the y-direction. The coupling efficiency of a dual ARROW-based structure can be controlled by adjusting the symmetric degree of structure which discussed in chapter 3. We can use this particular feature to design our device.

4.2 Design of the the Si-Based Sensor based on Dual ARROW Structures

In the vertical structure, we made the height 0.04 μm SiN_x strips (d_t) to increase the effective index in the lateral direction which are shown in Fig. 4.2 (b). The ARROW structure can be formed by these different effective indices. Following step, we deposited the silicon oxide to form the reference region and its thickness is 0.8 μm (d_p) which can ensure the effective index will not change in different environment (air and aqueous solution). After all process, We can get the effective index in the vertical direction. The N_{effH} was solved as $1.817 - 3.00 \times 10^{-11} j$ for TE polarization and N_{effL} was solved $1.773 - 1.58 \times 10^{-10} j$ for TE polarization in aqueous environment by using the Matlab program. Effective indices of the dual ARROW structure are shown in Table 4.2. Based on these parameters, we could calculate the lateral first cladding as 0.4 μm and the lateral second cladding as 1 μm if we chose lateral core width as 4 μm.

Table 4.2: The effective indices of the dual ARROW structure at the operation wavelength λ of 0.6328 μm.

	TE_0	TM_0
N_{effH}	$1.817 - 3.00 \times 10^{-11} j$	$1.744 - 5.86 \times 10^{-10} j$
N_{effL}	$1.773 - 1.58 \times 10^{-10} j$	$1.682 - 8.04 \times 10^{-9} j$

4.2.1 Design of the Input Region

Figure 4.3 shows the structure of the input region. At first, We designed the width of the lateral core (w_{g}) as 4 μm. Based on effective indices in the vertical direction, we can calculate widths of the lateral first cladding (w_{h}) as 0.4 μm and the lateral second cladding (w_{l}) as 1 μm by transverse antiresonant condition. Figure 4.4 shows the two-dimensional field profiles of the fundamental TM mode for one core with five antiresonant cavities in the y-direction and the propagation loss is almost zero (0.000047 dB/cm). Table 4.3 shows the propagation losses of the fundamental TM mode with different number of cavities.

Table 4.3: The relations between the number of cavities and the fundamental TM mode propagation loss. The unit of propagation loss is dB/cm

Number of cavities	1	2	3	4	5
Propagation losses	15.600	0.647	0.027	0.001	0.000

4.2.2 Design of the Coupling Region

The coupling region of dual ARROW structure and its corresponding effective indices are shown in Fig. 4.5. In the y-direction, the lateral first cladding (w_{h}) was calculated as 0.4 μm and the lateral second cladding (w_{l}) was calculated as 1 μm by the transverse antiresonant condition if we set the lateral core width as 4 μm. Figure 4.6 shows the field profiles of even and odd modes (E-field mainly in y-direction) in the dual ARROW structure with five cavities for TM polarization in the coupling

region. We can calculate the refractive indices of even and odd modes by Matlab which are 1.7713 - 1.80 $\times$ $10^{-10}j$ and 1.7712 - 1.89 $\times$ $10^{-10}j$, respectively. The coupling length was calculated as 3580 μm by the Eq. (3.3).

4.2.3 Design of the Decoupling Region

The decoupling region of dual ARROW structure and its corresponding effective indices are shown in Fig. 4.7. Because the coupling efficiency is strongly dependent on symmetric degree of the structure, we can easily construct the decoupling structure by digging the hole on the second core. In the vertical direction, the N_{effS} is calculated as $1.762 - 2.42 \times 10^{-10}j$ for TE mode and $1.653 - 3.17 \times 10^{-8}j$ for TM mode. Figure 4.8 shows field profiles of even and odd modes (E-field mainly in y-direction) in the dual ARROW structure with five cavities for TM polarization in the decoupling region.

4.2.4 Design of the Output Region

Figure 4.9 shows the structure of the output region. We designed the width of the output core (w_{go}) as 10.8 μm. Based on antiresonant condition, we can obtain widths of the lateral first cladding (w_{ho}) and the lateral second cladding (w_{lo}) as 0.4 μm and 5.4 μm, respectively. Figure 4.10 shows the two-dimensional field profile of the fundamental TM mode with nine antiresonant cavities in the y-direction and the propagation loss is zero.

4.3 Simulation Results of the the Si-Based Sensor based on Dual ARROW Structures

Before constructing the sensor device, performances of the coupling structure and the decoupling structure should be discussed first. Figure 4.11 shows the simulation result of the coupling region at the aqueous environment. The coupling efficiency of

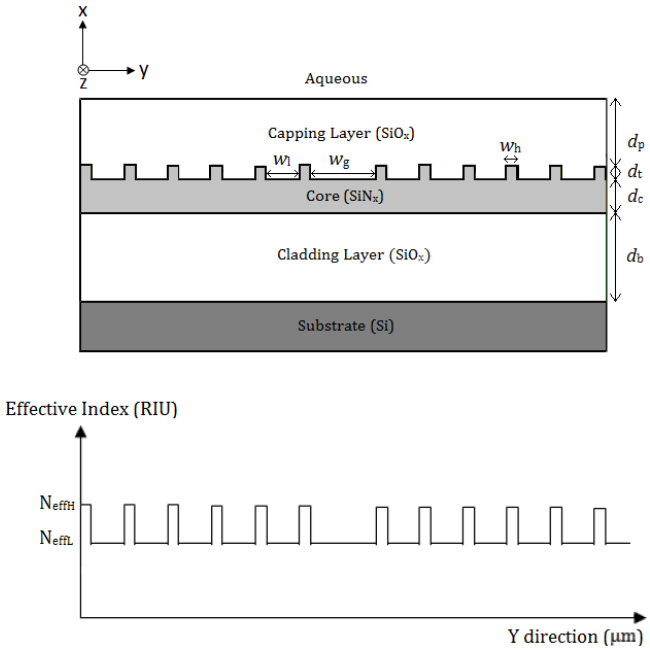

Figure 4.3: The cross section and the corresponding effective index profile of the input region.

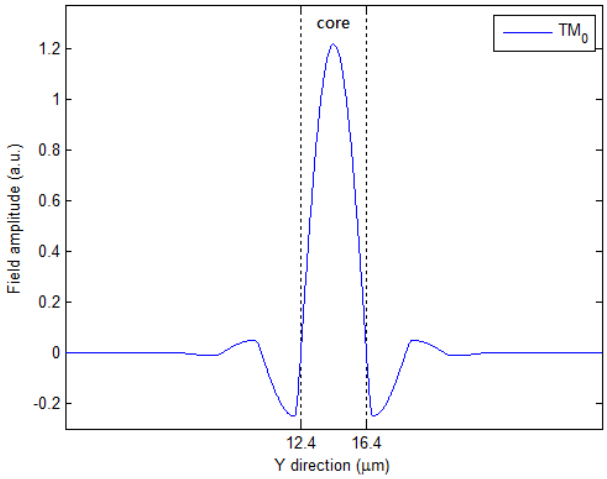

Figure 4.4: The two-dimentional field profile of the fundamental TM mode for one core with five antiresonant cavities.

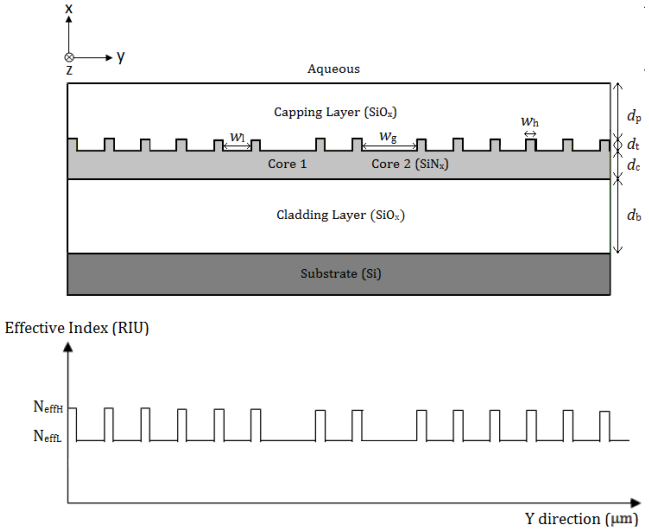

Figure 4.5: The two-dimentional field profile of the fundamental TM mode for one core with five antiresonant cavities.

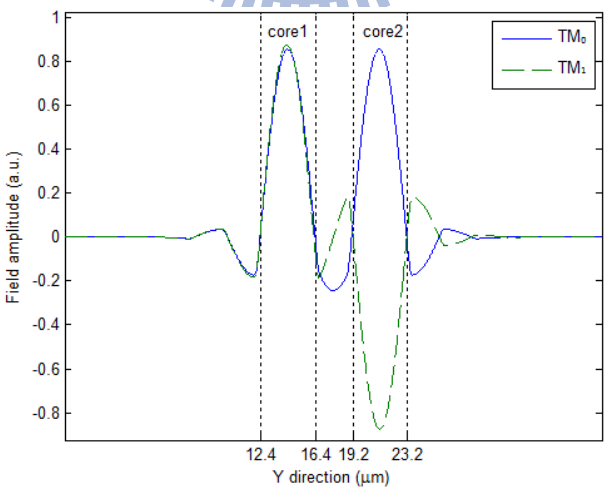

Figure 4.6: The two-dimensional field profiles of even and odd modes for TM polarization in the coupling region.

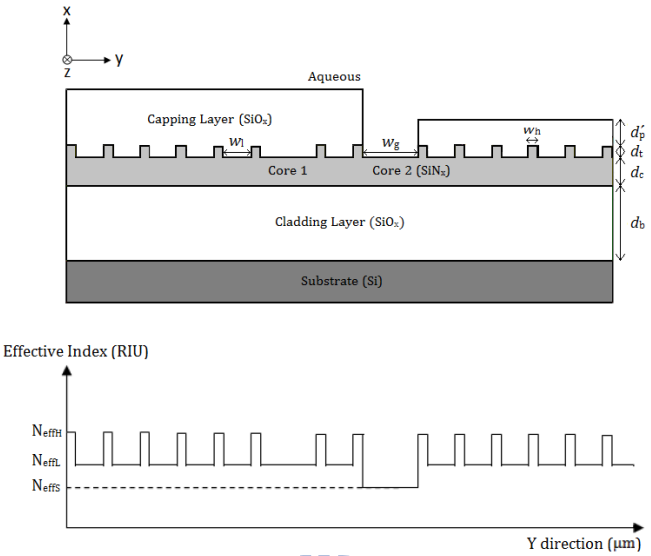

Figure 4.7: The two-dimensional field profiles of even and odd modes for TM polarization in the decoupling region.

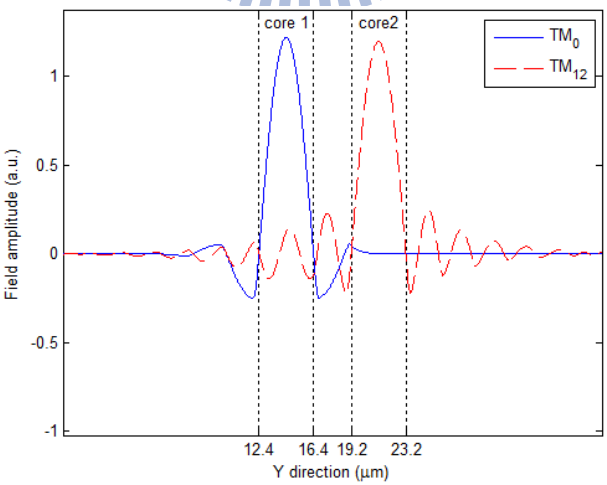

Figure 4.8: The two-dimensional field profiles of even and odd modes for TM polarization in the decoupling region.

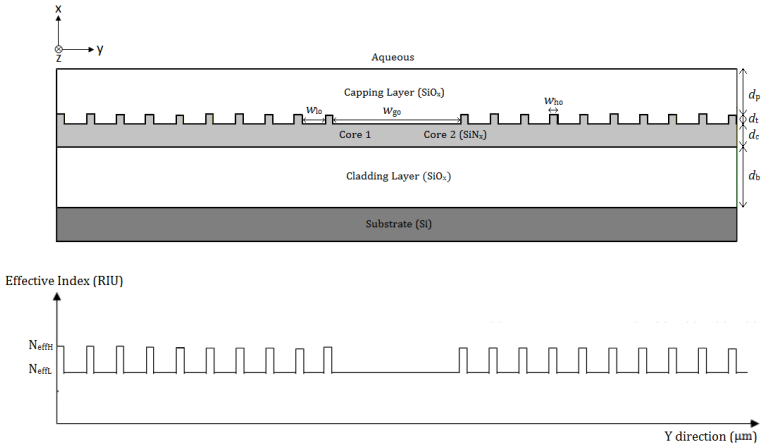

Figure 4.9: The cross section and the corresponding effective index profile of the output region.

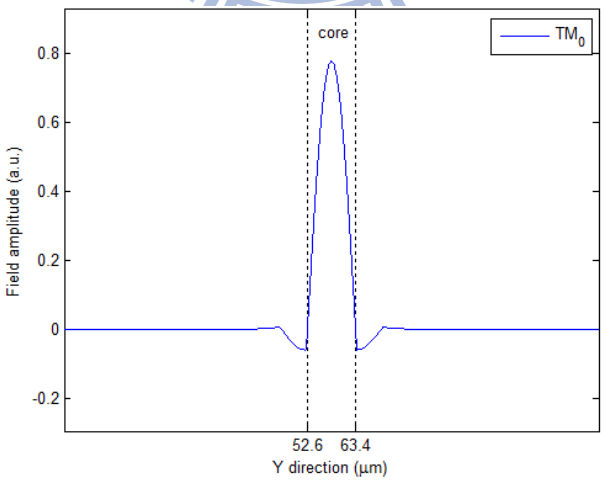

Figure 4.10: The cross section and the corresponding effective index profile of the output region.

the coupling region was calculated as 97.40% where the coupling efficiency is defined as $\Delta P_2(\mathrm{z})/P_1(0)$.

Figure 4.12 shows the simulation result of the decoupling region and the coupling efficiency is calculated as 0.06%.

Then we combine these structures in order of the input region, the coupling region, the decoupling region, and the output region as the Fig. 4.1 shows. The first region (input region) provides a condition which can stabilize the input field when the Gaussian beam was launched into the sensor device. The second region (coupling region) acts as 3dB-coupler which splits input field to two equal fields. The third region (decoupling region) is designed to be a sensing region. The fourth region (output region) is designed to receive the two lightwaves and detect the power.

In setting parameters, we chose lengths of the input region 2000 μm, the coupling region 1880 μm which is the length for splitting input field to two equal fields ($\sim L_c/2$), the decoupling region 2000 μm, and the output region 6120 μm. Figure 4.13 shows the BPM simulation result and Fig. 4.14 shows its sensitivity which is the power of the first core versus refractive index of environment.

4.4 Summary

An dual ARROW-based structure with its coupling feature can be designed as Mach-Zehnder-like sensor. Because the coupling behavior strongly depends on the degree of the structural symmetry, we can effectively control the coupling efficiency from near 100% to 0%. Thus, the compact sensor without any bending structure can be realized. The sensor based on dual ARROW structures can reach the sensitivity 475 a.u./RIU.

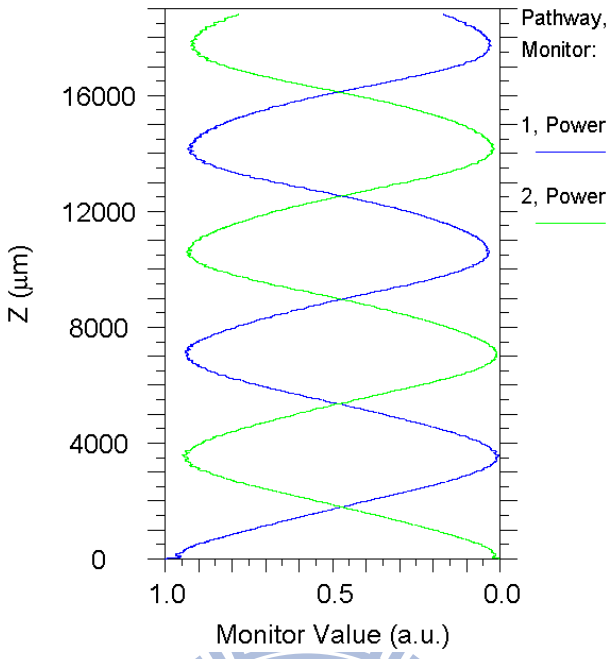

Figure 4.11: The BPM simulation of the coupling region

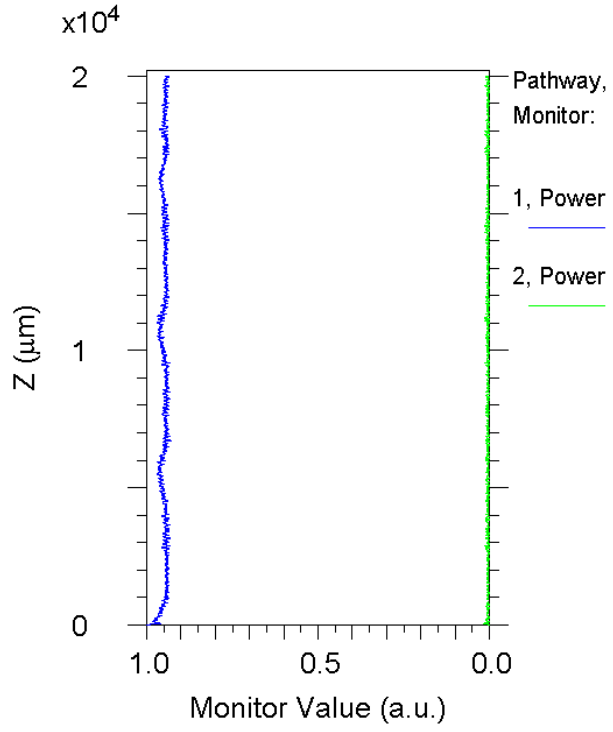

Figure 4.12: The BPM simulation of the decoupling region

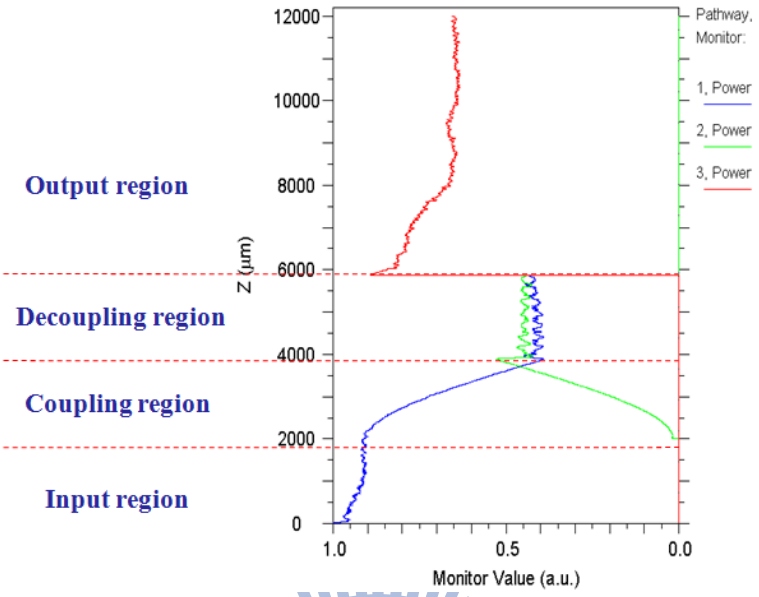

Figure 4.13: The BPM simulation of the Si-based sensor based on dual ARROW structures

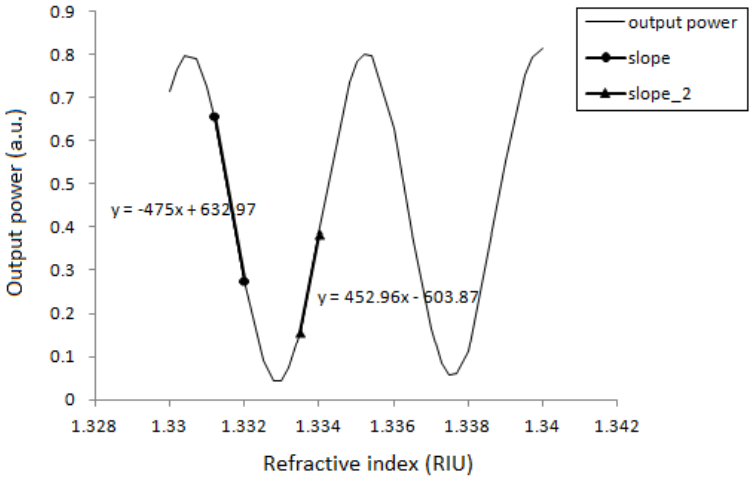

Figure 4.14: The sensitivity of the sensor based on Dual ARROW structures with the intput region (2000 μm), the coupling region (1880 μm), the decoupling region (2000μm), and the output region (6120 μm)

Chapter 5

Device Fabrication

5.1 Introduction

In this section, We mention the fabrication of the Si-based sensors based dual ARROW structures. We first made the zero mark and then deposited two layers which involve SiO_x and SiN_x films to form the slab waveguide in the vertical direction by the "Oxford PECVD" (Plasma- Enhanced Chemical Vapor Deposition). Next, we used "Clean Track MK-8 to coat photoresist (P.R.) and exposured by "Leica E-beam" (Leica weprint 200), and then the P.R. were developed to produce waveguide patterns. In the etching process, we utilized the "ILD-4100" to form our particular structure. Finally, we used the "Wet Bench to remove PR, and made the inspection by utilizing the "In-line SEM" (In-line Scanning Electron Microscopy). Figure 5.1 shows fabrication processes of the Si-based sensors based on dual ARROW structures. All the fabrication processes were completed in the NDL (National Nano Device Laboratories). The detailed fabrication parameters and process are discussed in the following sections.

5.2 Deposition

Before all deposition, due to multi-step processes, the zero mark should be made first. So we deposited the 3000 Å silicon oxide as the hard mask and etched the zero mark with the depth of Si substrate about 15000Å. Then we used wet bench to eliminate organic, inorganic attachment, and other contaminants.

we used the chamber A of the Oxford PECVD system to deposit SiO_x film as my lower cladding layer. The PECVD system can deposit films with lower stress, and the deposition rate is faster than a horizontal furnace system. Moreover, the PECVD system produces oxide films with high uniformity and low viscosity at a low deposition temperature.

The designed thickness of the lower cladding layer (SiO_x) is 1 μm and the parameter is shown in Table 5.1. The chemical reaction is

$$3SiH_4 + 6N_2O \rightarrow 3SiO_2 + 4N_2 + 4NH_3 \tag{5.1}$$

Table 5.1: The parameter of the lower cladding layer oxide.

Time (sec)	875
N_2 (sccm)	161.5
N_2O (sccm)	710
SiH_4 (sccm)	8.5
RF power (W)	20
Pressure (mTorr)	1000
Temperature (°C)	300

Then we used "N&K 1200" to measure the thicknesses and indices which is a popular thin film measurement system based on the patented N&K method. The method is used to calculate the thickness and the refractive index of thin films by utilizing Forouhi and Bloomer dispersion equations based on quantum mechanics.

Following, we deposited 0.22 μm silicon nitride as the core material by Oxford PECVD. The deposition parameters are listed in Table 5.2. Its chemical reaction is

$$3SiH_4 + 4NH_3 \rightarrow Si_3N_4 + 12H_2 \tag{5.2}$$

Table 5.2: The parameter of the lower cladding layer oxide.

Time (sec)	264
N_2 (sccm)	980
NH_3 (sccm)	20
SiH_4 (sccm)	20
RF power (W)	20
Pressure (mTorr)	850
Temperature (°C)	300

Table 5.3 shows the measurement results including lower cladding layer silicon oxide (SiO_x) and core layer silicon nitride (SiN_x). And the five points are shown in Fig. 5.2 . After first lithography, we deposited 0.8 μm as the capping layer which prevents the lightwave form external environment in each reference region.

Table 5.3: The parameter of the lower cladding layer oxide.

Meterial	SiO_x	SiN_x
Thickness / Refractive index	d (μm) / n	d (μm) / n
Location 1	1.03 / 1.472	0.21 / 2.075
Location 2	1.01 / 1.472	0.21 / 2.071
Location 3	1.00 / 1.471	0.21 / 2.072
Location 4	1.01 / 1.472	0.21 / 2.074
Location 5	1.01 / 1.472	0.21 / 2.069
Average	1.01 / 1.472	0.21 / 2.072

5.3 Lithography

Figure 5.3 shows the layout pattern of dual ARROW-based sensors. R-soft was used to simulate the situation of beam propagation and L-edit was used to convert the

pattern to gds file which can be read by lithography system. In the dual ARROW-based sensor, it was divide into four parts including the input region, the coupling region, the decoupling region, and the output region. After completing the core layer deposition, we used the "Clean Track MK-8" system to carry out lithography processes. Before deliver the wafer into track, we used the stress measurement instrument to measure the radius of curvature of the wafer which can show the stress degree of the wafer. If the wafer was bended too much, the machine arm of the exposure system (Leica E-beam) could not grab it. Then we mention the lithography procedure in order of the track steps:

a. HMDS coating: At first, we added the HMDS, $((CH_3)_3SiNHSi(CH_3)_3)$, on the wafer surface for enhancing the adhesion between the wafer and the photoresist.

b. Pre-bake: Then, we deliver the wafer into the hot plate unit, which the temperature is 90 °C and the baking time is 60 seconds, in order to volatilize the excess aqueous solution.

c. Photoresist coating: After cooling the wafer, the photoresist was applied. Initially, the speed of spin coating should be slow for the photoresist spread uniformly on the wafer surface and then raise speed to achieve the thickness which we want. The first spin speed was set at 500 rpm for 10 seconds and the second spin speed was set at 5000 rpm for 45 seconds where the final thickness of negative photoresist is 3800 Å.

d. Soft bake: Then, in order to remove the excess solvent of photoresist and enhance the adhesion between dielectrics, we deliver the wafer into hot plate unit again. The temperature of the step is 90 °C and the baking time is 90 seconds.

e. Exposure: After cooling, the wafer transferred to "Leica E-beam" (Leica weprint 200) to exposure.

f. Post Exposure Bake: To eliminate standing wave effect and promote the light-acid diffusion, the wafer delivers to hot plate unit again.

g. Development: After exposure, we transferred the wafer to "Clean Track MK-8"to develop the P.R..

h. Hot bake: To remove excess solvents which come from development process, the wafer delivers to hot plate unit to achieve this requirement. The temperature of this step is 120 °C and the baking time is 90 seconds.

i. Inspection: Finally, we used the in-line SEM (in-line scanning electron microscopy) to inspect the lithography results.

5.4 Etching Process and After Etching Inspection (AEI)

In etching process, it divided four-step etchings. The first etching process, which was after the deposition of the 2200 Å core layer (silicon nitride), we etched silicon nitride 400 Å to make antiresonant cavities along the y direction. The etching recipes are shown in Table 5.4. The Ar gas in this recipe was used to produce plasma. CHF_3 was used to produce polymers and CF_4 was used to produce the ions of fluorine. The ions of fluorine were used to etch the designed segment. For the second etching process, which was after the deposition of the 8000 Å capping layer (silicon oxide), we etched silicon oxide 4000 Å upon the second core (right core) and recipes were all the same to the first etching but only etching time was edited to 180 seconds.

For the third etching process which was after the second etching process, we etched the silicon oxide 4000 Å again to make the liquid could flow to the groove which was upon the second core. The difference between second and third etching

Table 5.4: The recipe for etching core layer (SiN_x) 400 Å by the metal etcher.

Step	
Time (sec)	21
Gas stab / exha (sec)	60 / 20
RF / Bias power (W)	500 / 50
Pressure (mTorr)	8.5
CF_4 (sccm)	80
CHF_3 (sccm)	80
ESC / He flow (V / cc)	450 / 4
Magnet 1 / 2 (A)	41 / 35
Holder position	3
Circulator (°C)	60 / 60

process was the mask layout. The third mask layout was cross over to second core and antiresonant cavities which were next the right side of the second core. We used the wet bench system to remove the residual photoresist on the wafer with the chemical solution of H_2SO_4 : H_2O_2 = 3 : 1 at 120 °C for 10 minutes. After etching inspection (AEI) images were photographed by the TF-SEM (Thermal Field Emission Scanning Electron Microscopy) to measure the depth and width whether we want or not.

Figure 5.4, Fig. 5.5, and Fig. 5.6 show topviews of the input region, which are widths of the core, the first cladding, and the second cladding, respectively. Figure 5.7 shows the topview of the decouplng region, and Fig. 5.8 shows the core width in the decoupling region. Figure 5.9 and Fig. 5.10 show the cross-section views of the input region and the decoupling region.


Substrate
Bare Silicon
3000A SiOx
Substrate
Silicon Oxide Deposition as the Hard Mask by Oxford PECVD
3000A SiOx
Substrate
Photoresist Coating by Track
3000A SiOx
Substrate
Exposure by Leica E-beam and Development by Track
3000A SiOx
Substrate
Etching Oxide by Metal Etcher
3000A SiOx
Substrate
Remove Photoresist by Wet Bench
1200A SiOx
Substrate
Zero Mark Formation by Metal Etcher
Substrate
Remove Oxide by Wet Bench (BOE dipping 10mins)
Cladding Layer (SiOx)
10000A
Substrate
10000A Silicon Oxide Deposition as Bottom Layer by Oxford PECVD
Core 1 SiNx Core 2
2200A
Cladding Layer (SiOx)
10000A
Substrate
2200A Silicon Nitride Deposition as Core Layer by PD220 PECVD (NFC)
Core 1 SiNx Core 2
2200A
Cladding Layer (SiOx)
10000A
Substrate
Photoresist Coating by Track
Core 1 SiNx Core 2
2200A
Cladding Layer (SiOx)
10000A
Substrate
Exposure by Leica E-beam and Development by Track
Core 1 SiNx Core 2
400A
1800A
Cladding Layer (SiOx)
10000A
Substrate
Etching Silicon Nitride 400A by Metal Etcher
Core 1 SiNx Core 2
400A
1800A
Cladding Layer (SiOx)
10000A
Substrate
Remove Photoresist by Wet Bench (H2SO4 dipping 10mins)

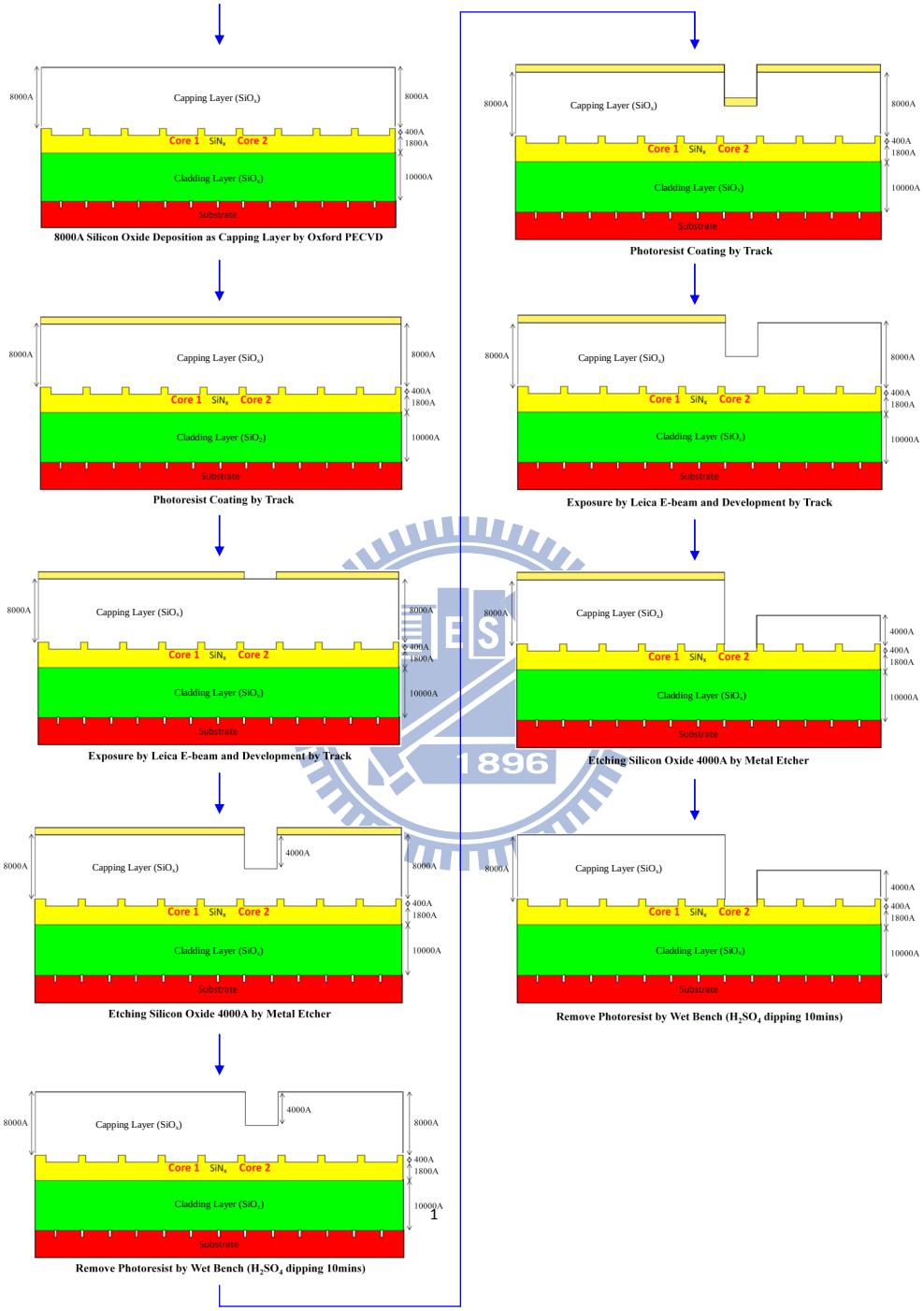

Figure 5.1: Flow chart of fabrication process for the Si-based sensor based on dual ARROW structures.

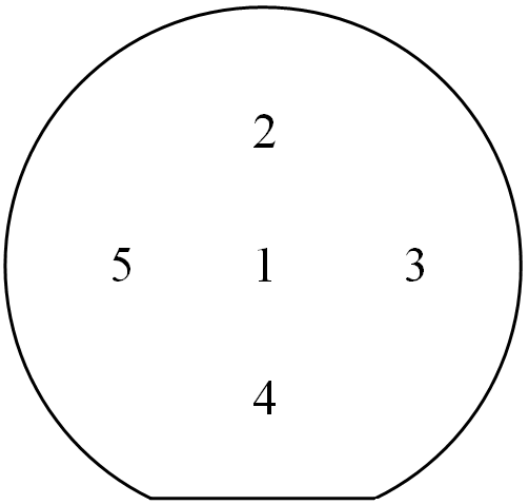

Figure 5.2: The locations of measuring points on a 6-inch Si wafer.

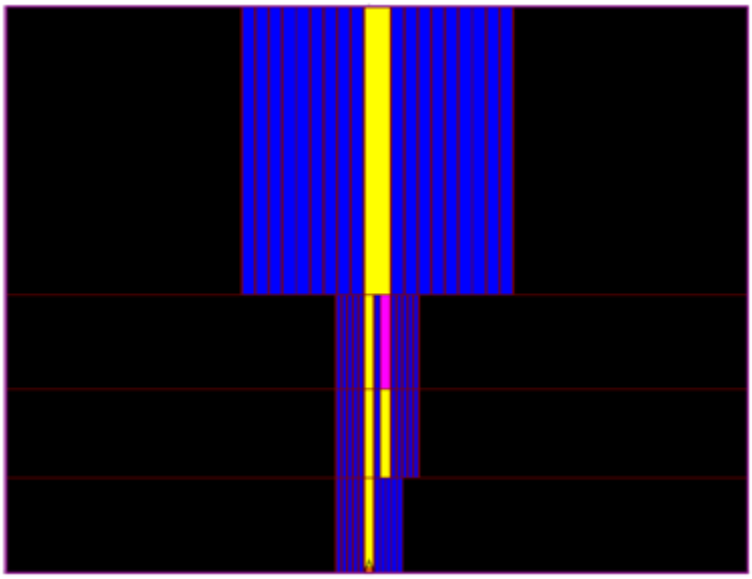

Figure 5.3: The layout of the Si-based sensor based on dual ARROW structures.

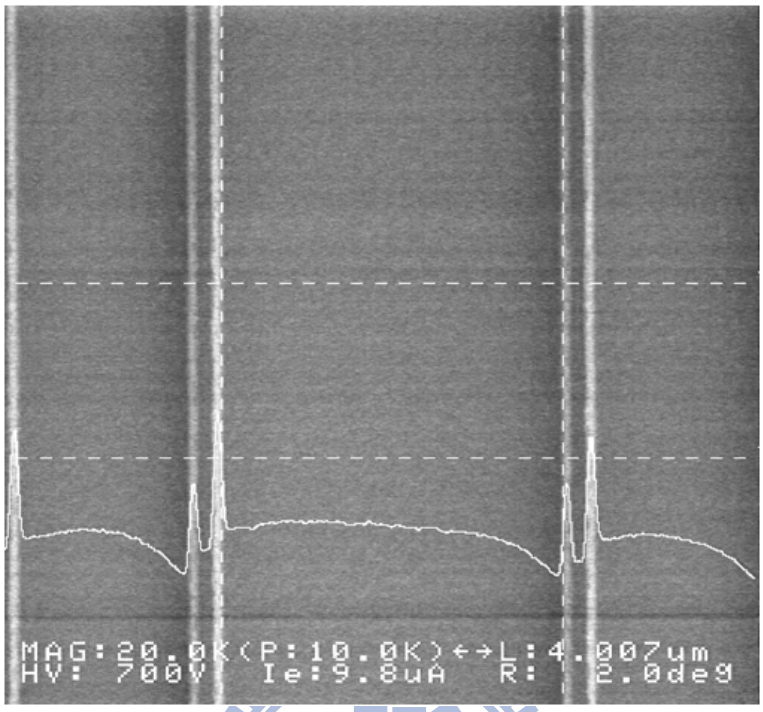

Figure 5.4: The width of the core in the input region.

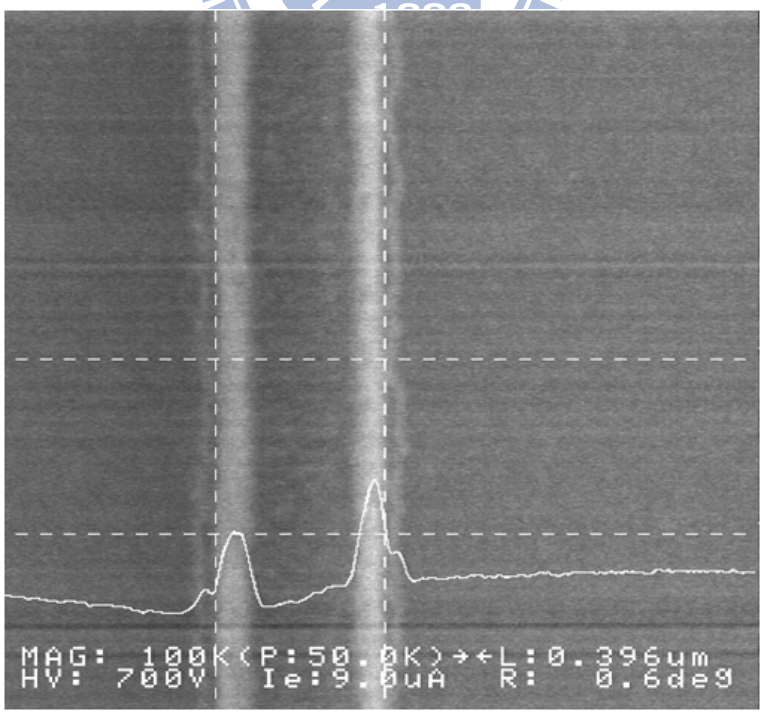

Figure 5.5: The width of the first cladding in the input region.

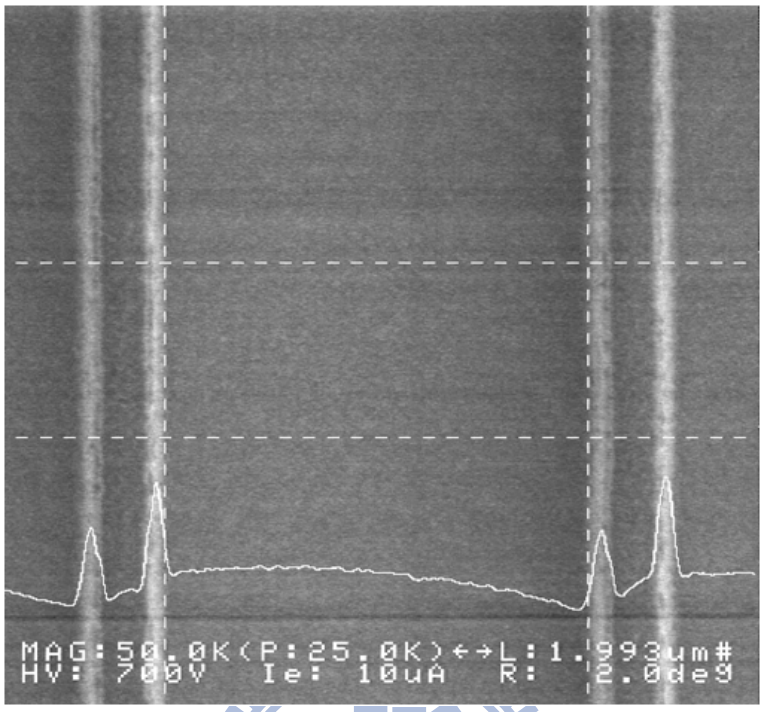

Figure 5.6: The width of the second cladding in the input region.

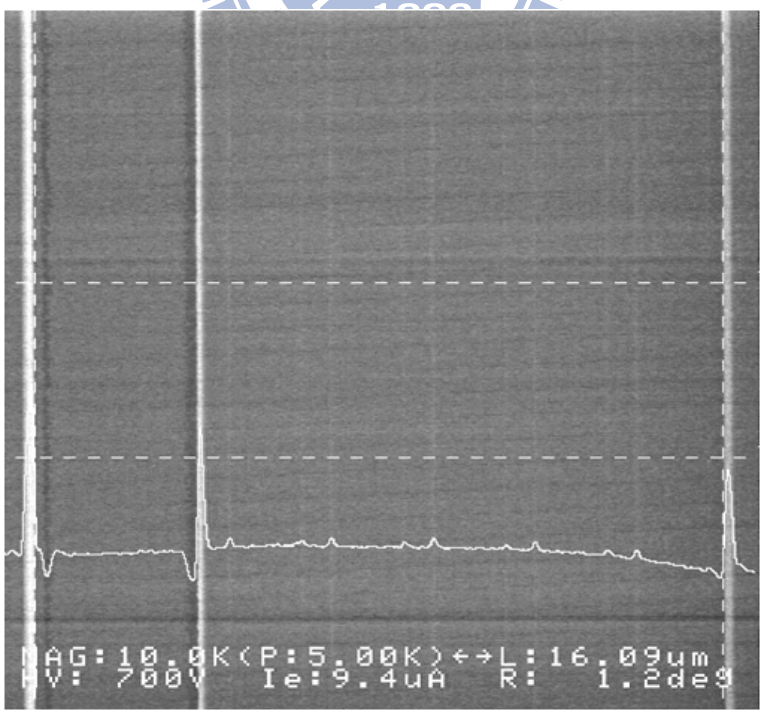

Figure 5.7: The topview of the decoupling region.

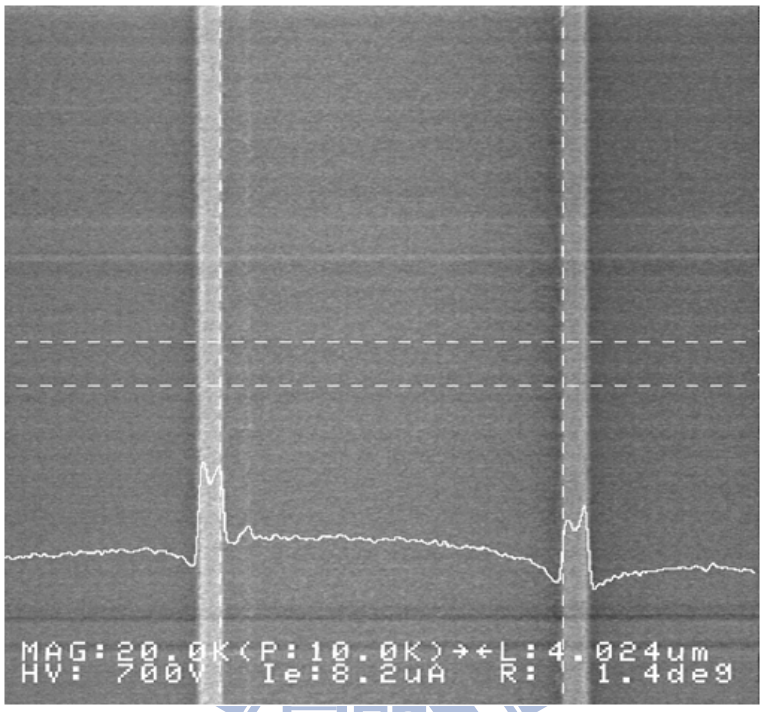

Figure 5.8: The width of the core in the decoupling region.

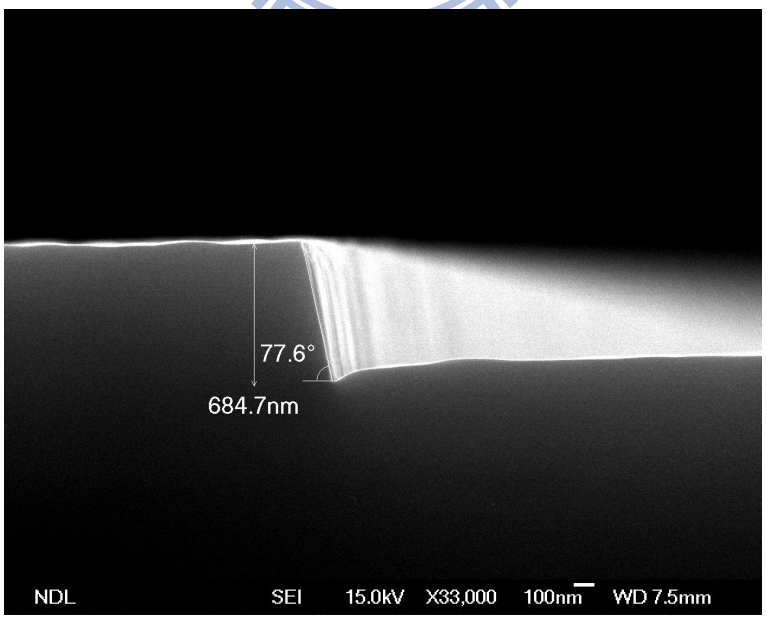

Figure 5.9: The cross-section view of the input region.

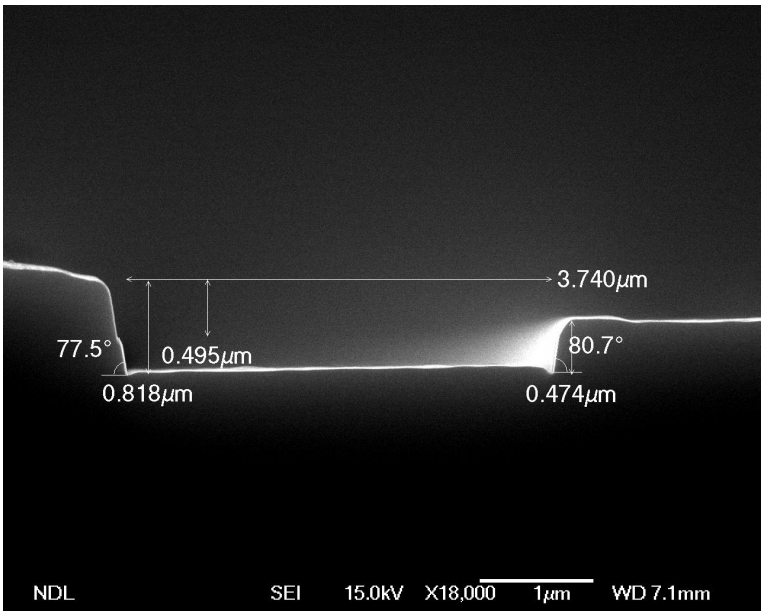

Figure 5.10: The cross-section view of the decoupling region.

Chapter 6

Measurement and Analysis

The concept and design of Si-based sensors based on dual ARROW structures have been investigated. The unique feature of dual ARROW structures, such as remote coupling and coupling efficiency tunability, can construct a bending-free and compact sensor device so that achieve the characteristics of miniaturization [35]. The theoretical analysis of the Si-based sensor has been carried out by employing the transfer matrix method and the eigenmode expansion. The parameters of the sensor structure have been also designed for aqueous solution detection. To confirm the function and characteristics, the measurement of various NaCl solutions would be presented.

6.1 The Setup of the Optical Measurement System

Due to the small core size (0.18 μm), the coupling loss is so large that the measurement is hard to execute if we launched He Ne laser to device directly (the spot diameter of the He-Ne laser is 0.65 mm). We used the lensed fibers (the average of spot diameter is 2.18 μm) to perform the experiments for characterizing the performance of our designed devices at the operation wavelength λ of 0.6328 μm. The configuration of optical measurement setup is illustrated in Fig. 6.1.

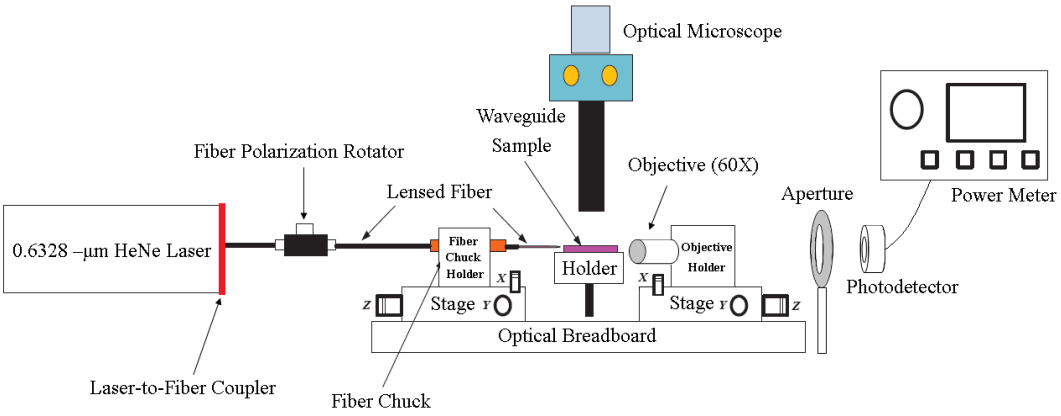

Figure 6.1: The configuration of optical measurement setup.

The optical measurement instruments contain:

(1) 0.6328-μm He-Ne laser: It supplies the light source with with $\lambda = 0.6328$ μm.

(2) Laser-to-fiber coupler: It supplies the transformation between laser to fiber.

(3) Lensed fiber: A general instrument providing a convenient way to improve coupling between an optical fiber and a waveguide device.

(4) Fiber polarization rotator: The instrument contains a rotatable plate polarizer for 0.6328 μm and PM fiber on both ends.

(5) Optical microscope (OM): It assists the alignment between the fiber and the input port of the waveguide.

(6) Microscope objective (60X): The instrument is used to receive the light from waveguide device.

(7) Aperture: It can filter out stray and radiative light noise, passing the primary light from the waveguide output to the power meter.

(8) Photodetector: It is used to detect the optical power.

(9) Power meter: It shows the power intensity.

The optical measurement setup is shown in Fig. 6.2. In the optical system, the He-Ne laser with a wavelength of 0.6328 μm was used as the light source. We used the fiber polarization rotator to keep only the TE-polarized light could pass, and utilized the lensed fiber to couple the light into the input port of the sensor device.

At the output end, the output beam was focused by an objective lens (60X) and passed through an aperture to filter out the radiative light noise. Then, the photodetector collected light signal and power meter recorded the measurement data. In aligning step, we tuned the x, y, and z positions of the stage until the clear light spot appeared, as shown in Fig. 6.3. An optical microscope (OM) were used to alignment at the input port. The stringent requirement for end-face flatness and alignment accuracy are necessary for this measurement system.

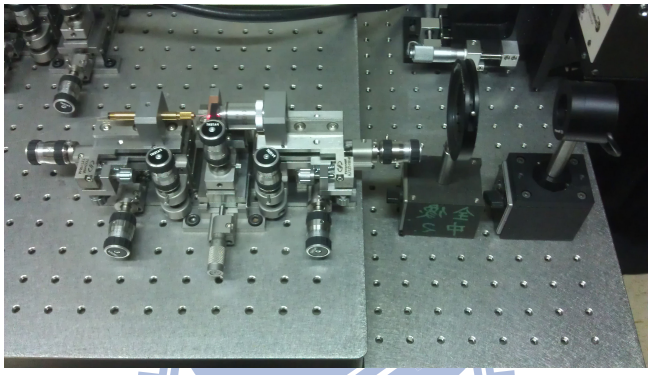

Figure 6.2: The optical measurement setup.

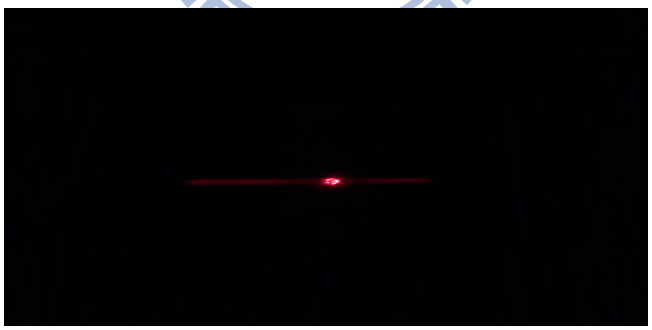

Figure 6.3: The image of the light spot form the output port of the Si-based sensor based on dual ARROW structures.

6.2 Measurement of NaCl Solutions

In order to demonstrate the performance of Si-based sensors based on dual ARROW structures, we measured the output power and injected different NaCl concentration

at the same time. The optical measurement setup is shown in Fig. 6.4. The NaCl concentration were 0.05M, 0.10M, 0.15M, 0.20M, 0.25M, 0.30M, 0.35M, 0.40M, 0.45M, and 0.50M. The corresponding refractive indices were about 1.3355, 1.3360, 1.3370, 1.3375, 1.3378, 1.3380, 1.3385, 1.3390, 1.3395, and 1.3400, respectively. The measurement results of chip 1, chip 2, chip 3, chip 4, chip 5, and chip 6 were shown in Fig. 6.5, Fig. 6.7, Fig. 6.9, Fig. 6.11, Fig. 6.13, and Fig. 6.15. These figures show that power changes as the refractive index of NaCl solutions changes. We captured each period output power of NaCl solution to get the average output power and shown in Fig. 6.6, Fig. 6.8, Fig. 6.10, Fig. 6.12, Fig. 6.13, and Fig. 6.16. In additional, to verify the repeatability and the consistency, we measured the chip 6 again with the NaCl concentration 0.21M, 0.23M, 0.27M, 0.29M, 0.31M, and 0.33M. Its corresponding refractive indices were about 1.3375, 1.3375, 1.3378, 1.3380, 1.3380, 1.3380, and 1.3385. The measurement result was shown in Fig. 6.17 and the average output power with different NaCl concentration was shown in Fig. 6.19. According to the measurement result of chip 6, we can get the average sensitivity 1305 μW/RIU in the range 1.3375 to 1.3380, which shown in Fig. 6.20 and Fig. 6.21.

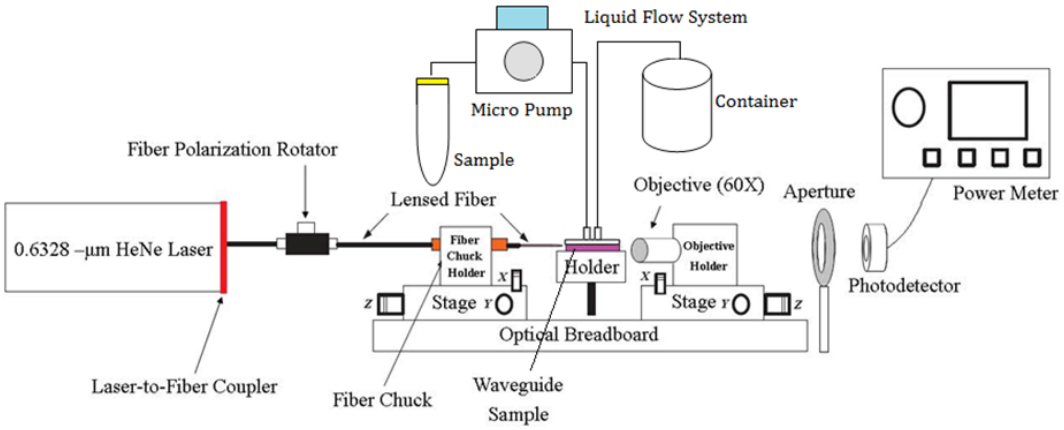

Figure 6.4: The optical measurement setup with the liquid flow system.

6.3 Discussion

The sensor based on dual ARROW designed for aqueous environment have been investigated. To verify the performance, we measure it with different concentration of NaCl solutions (0.05M, 0.10M, 0.15M, 0.20M, 0.25M, 0.30M, 0.35M, 0.40M, 0.45M, and 0.50M). The measurement results shown in Fig. 6.5, Fig. 6.7, and Fig. 6.9, Fig. 6.10, Fig. 6.12, and Fig. 6.14. The sensitivity of detecting the environmental refractive index change by the sensor was 1305 μW/RIU (for chip 6 case), which is much lower than simulation (2312800 μW/RIU). Some reasons will be discussed:

(1) The coupling efficiency between laser and fiber is too small. Even though the power of He-Ne laser is detected about 15 mW, but, when we connect the laser-to-fiber coupler to He-Ne laser, the power will decrease to about 1 mW.

(2) The loss between rotator is too large. When we launched the 1 mW light, the power will decrease to 200 μW as the light passed rotator and lensed fiber.

(3) The coupling loss between lensed fiber and device is still present.

(4) The imperfect fabrication will induce large loss among the device.

So, if we want to reach high sensitivity, the maintenance of the power which launched form He-Ne laser is a primary issue should be overcome. However, a novel Si-based sensor without any bending structure is realized.

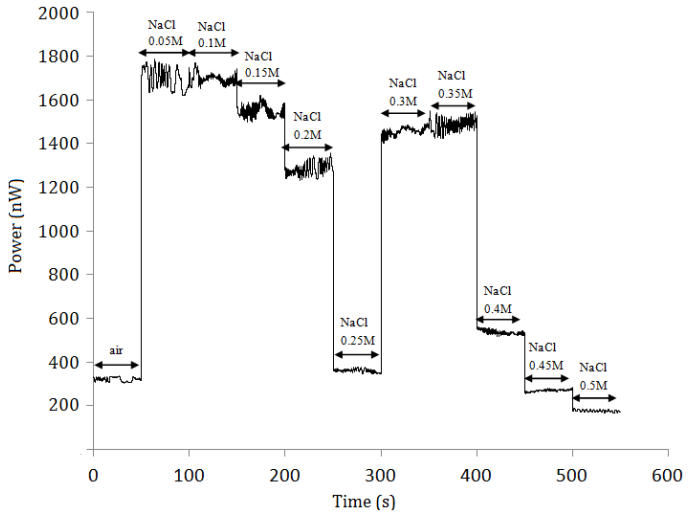

Figure 6.5: Sensorgram of the Si-based sensor based on dual ARROW structures (chip 1), when NaCl solutions were flowed across the sensor surface. The concentration of NaCl solutions were 0.05M, 0.10M, 0.15M, 0.20M, 0.25M, 0.30M, 0.35M, 0.40M, 0.45M, and 0.50M.

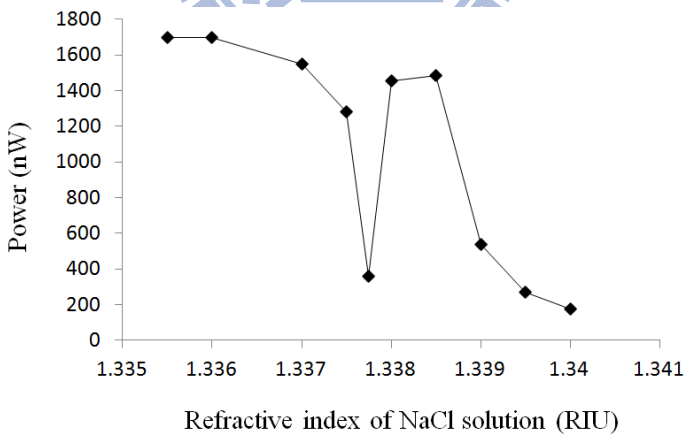

Figure 6.6: Statistic analysis of the average power (chip 1).

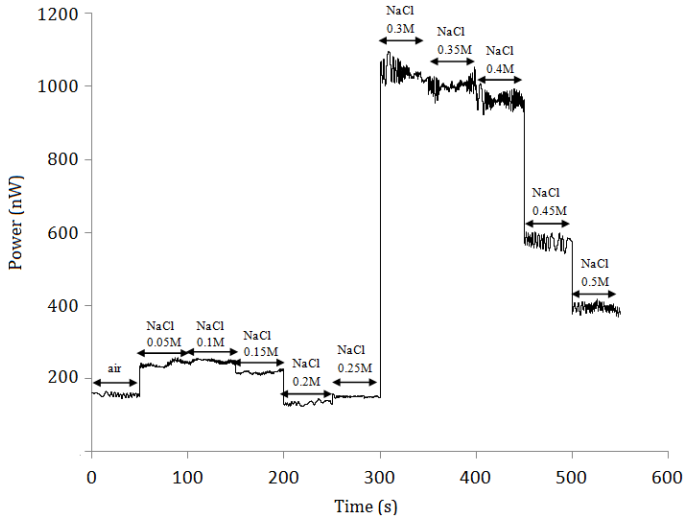

Figure 6.7: Sensorgram of the Si-based sensor based on dual ARROW structures (chip 2), when NaCl solutions were flowed across the sensor surface. The concentration of NaCl solutions were 0.05M, 0.10M, 0.15M, 0.20M, 0.25M, 0.30M, 0.35M, 0.40M, 0.45M, and 0.50M.

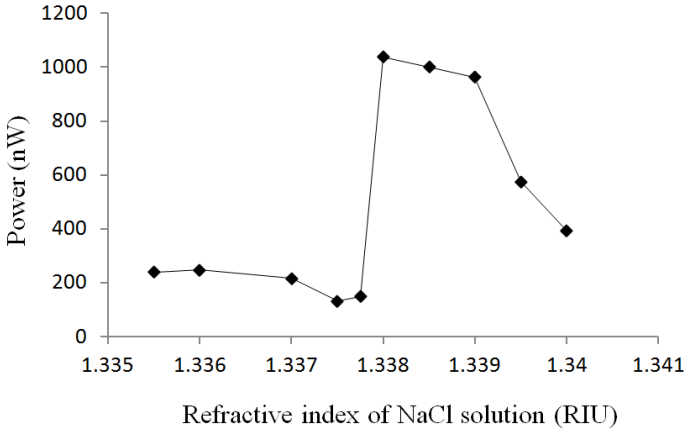

Figure 6.8: Statistic analysis of the average power (chip 2).

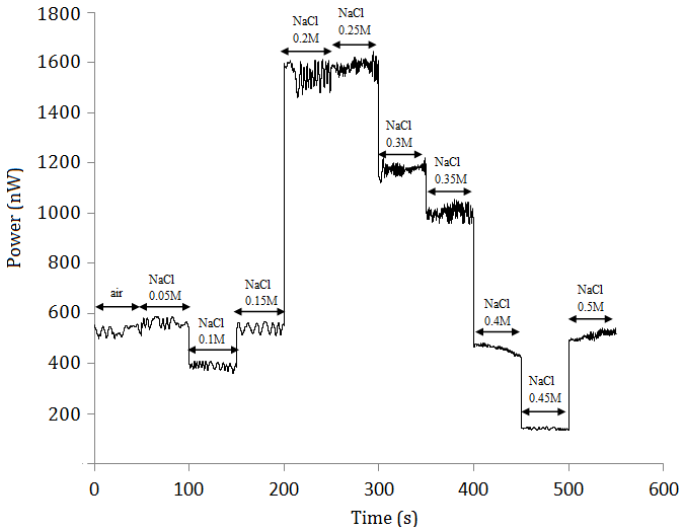

Figure 6.9: Sensorgram of the Si-based sensor based on dual ARROW structures (chip 3), when NaCl solutions were flowed across the sensor surface. The concentration of NaCl solutions were 0.05M, 0.10M, 0.15M, 0.20M, 0.25M, 0.30M, 0.35M, 0.40M, 0.45M, and 0.50M.

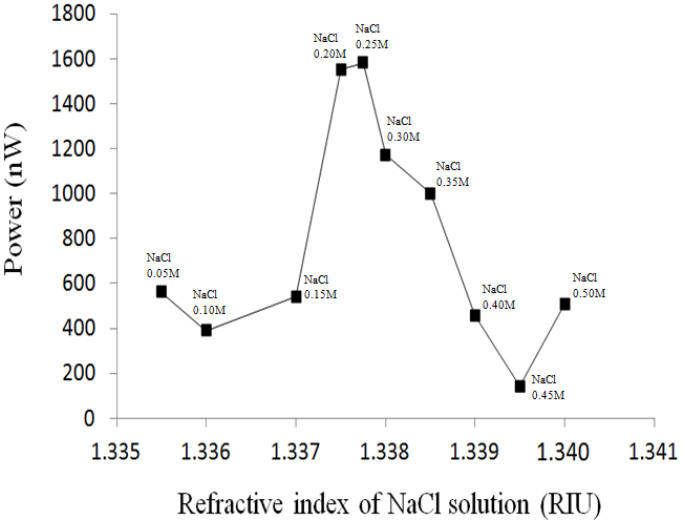

Figure 6.10: Statistic analysis of the average power (chip 3).

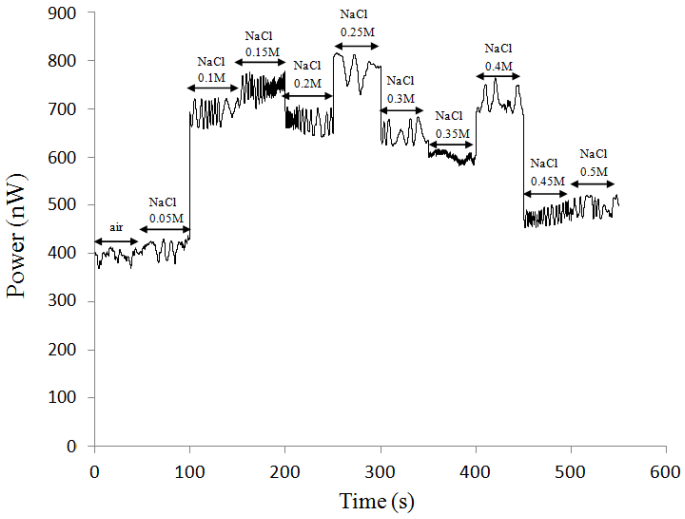

Figure 6.11: Sensorgram of the Si-based sensor based on dual ARROW structures (chip 4), when NaCl solutions were flowed across the sensor surface. The concentration of NaCl solutions were 0.05M, 0.10M, 0.15M, 0.20M, 0.25M, 0.30M, 0.35M, 0.40M, 0.45M, and 0.50M.

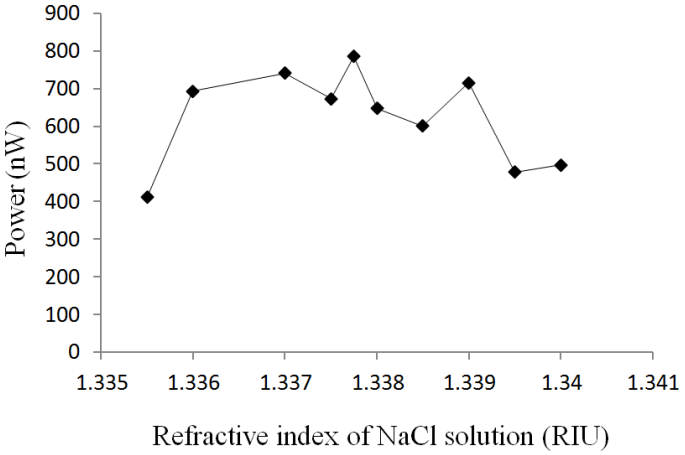

Figure 6.12: Statistic analysis of the average power (chip 4).

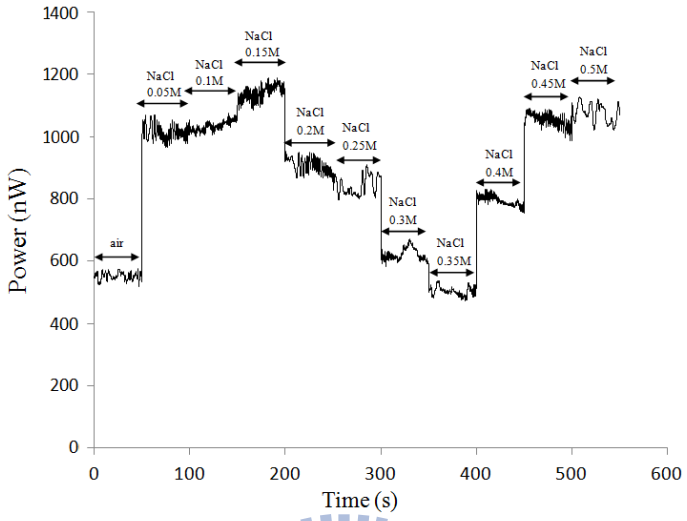

Figure 6.13: Sensorgram of the Si-based sensor based on dual ARROW structures (chip 5), when NaCl solutions were flowed across the sensor surface. The concentration of NaCl solutions were 0.05M, 0.10M, 0.15M, 0.20M, 0.25M, 0.30M, 0.35M, 0.40M, 0.45M, and 0.50M.

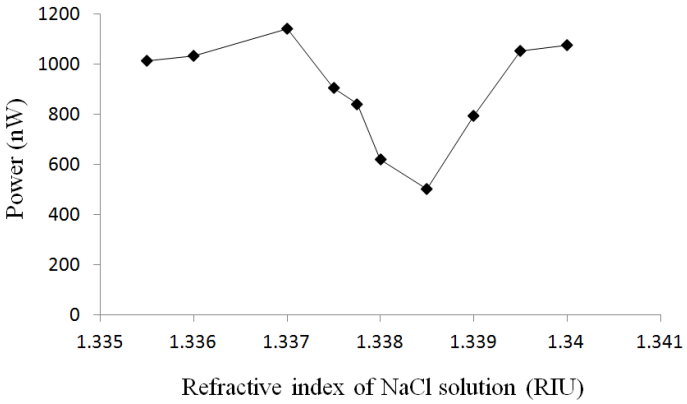

Figure 6.14: Statistic analysis of the average power (chip 5).

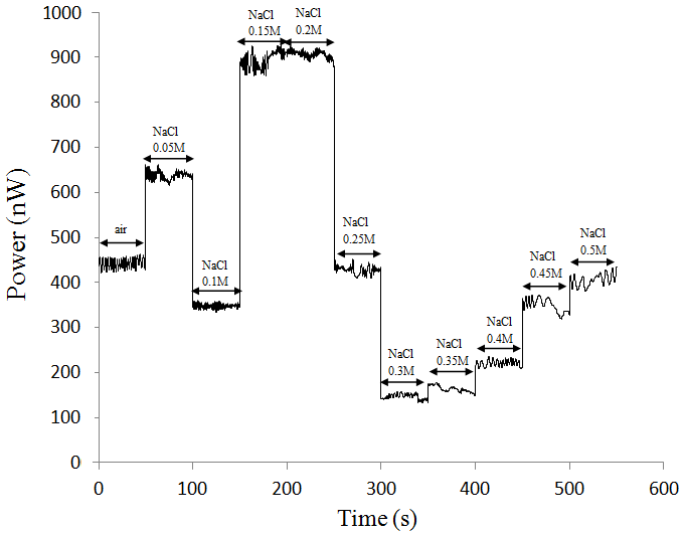

Figure 6.15: Sensorgram of the Si-based sensor based on dual ARROW structures (chip 6), when NaCl solutions were flowed across the sensor surface. The concentration of NaCl solutions were 0.05M, 0.10M, 0.15M, 0.20M, 0.25M, 0.30M, 0.35M, 0.40M, 0.45M, and 0.50M.

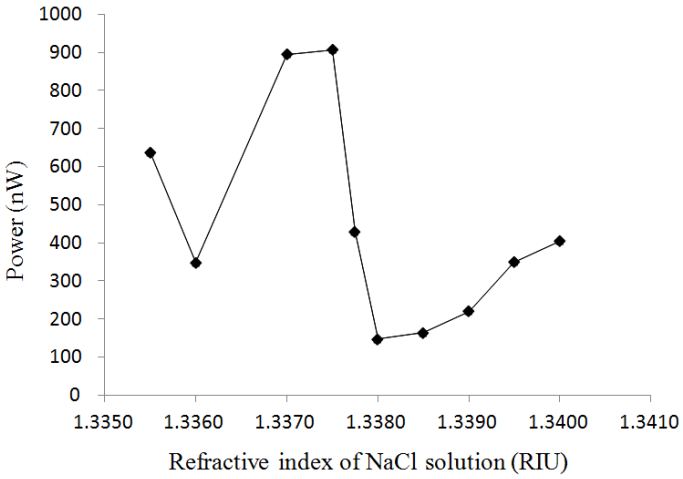

Figure 6.16: Statistic analysis of the average power (chip 6).

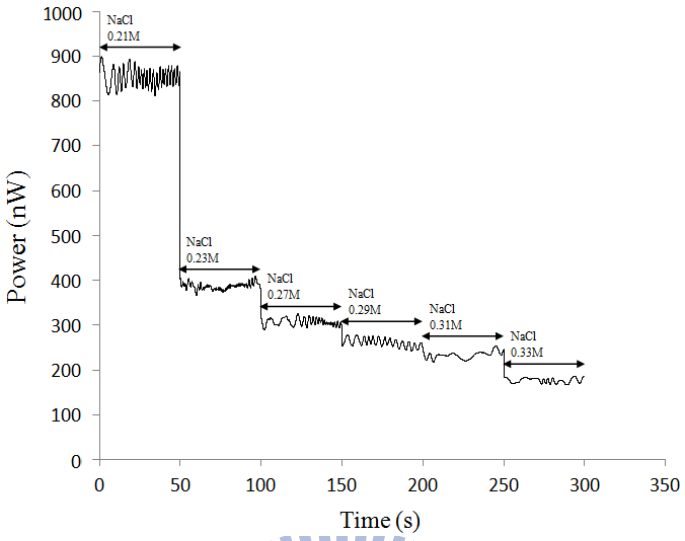

Figure 6.17: Sensorgram of the Si-based sensor based on dual ARROW structures (chip 4), when NaCl solutions were flowed across the sensor surface. The concentration of NaCl solutions were 0.21M, 0.23M, 0.27M, 0.29M, 0.31M, and 0.33M.

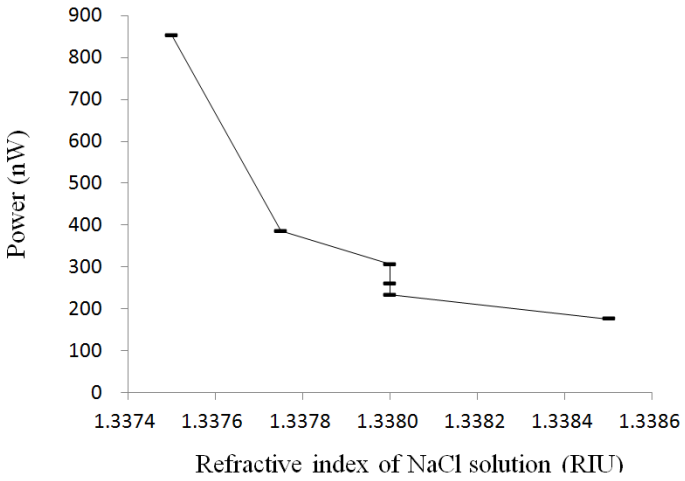

Figure 6.18: Statistic analysis of the average power (chip 6).

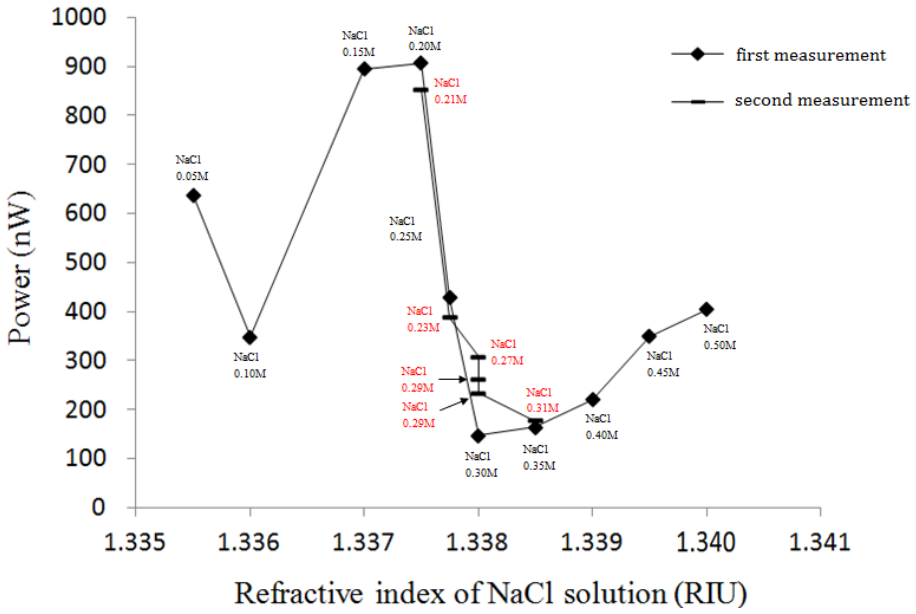

Figure 6.19: Statistic analysis of the average power with twice measurements on the same chip (chip 6).

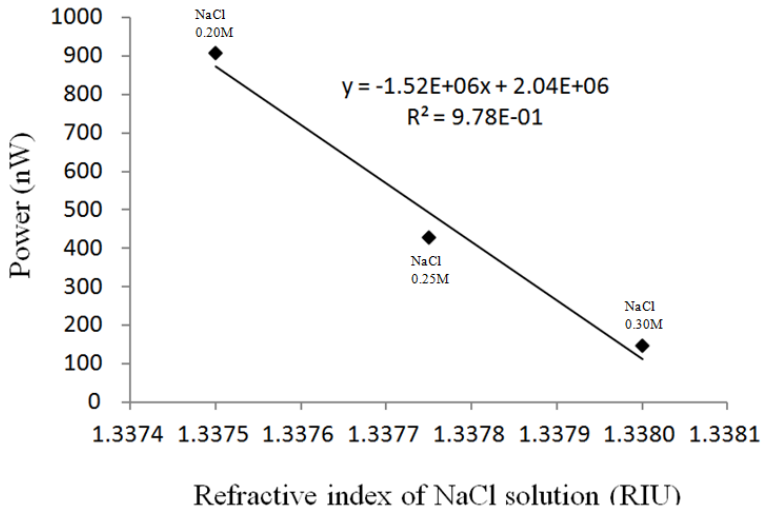

Figure 6.20: Statistic analysis of the average power difference (chip 6).

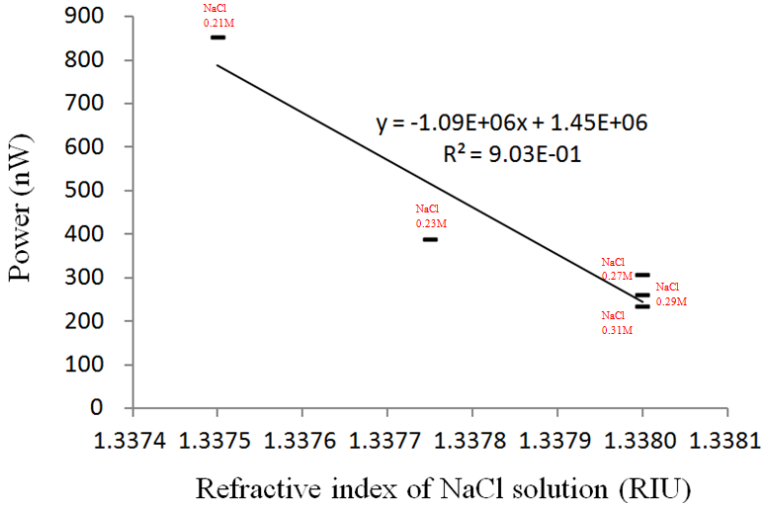

Figure 6.21: Statistic analysis of the average power difference (chip 6).

Chapter 7

Conclusion

In this study, the design, fabrication, and characterization of Si-based sensors based on dual ARROW structures have been investigated. The theoretical analysis of dual ARROW-based sensors has been carried out by employing the transfer matrix method (TMM), the effective index method (EIM), the eigenmode propagation analysis, and the beam propagation method (BPM). In the vertical x-direction, a conventional waveguide employing silicon nitride as the core material and silicon dioxide as the lower cladding layer was used. The thickness of the core layer was designed as 0.18 μm which is in accordance with cutoff condition for single-mode propagation, and the thickness of the lower cladding layer was designed as 1 μm. In the lateral y-direction, dual ARROW-type structures fulfilled by a series of the strips were used for constracting a compact sensor. To attain a low propagation loss for the fundamental mode, all the widths of the strips w_{h} and the distances w_{l} between the strips except the core width w_{g} must satisfy the transverse antiresonance condition.

Based on the maximum coupling efficiency analysis, it is found that a dual ARROW can operate as a directional coupler or as two decoupled waveguides by controlling the structural symmetry. With these features, coupled and decoupled structures can be designed to have the same separation width. In our designed structure, we

connected a input structure which was designed to stabilize the input field and dual-ARROW 3-dB couplers with a decoupled dual-ARROW structure, and combined with a output structure which was designed to receive lightwave from decoupled structure. The compact sensor without any lengthy bends can be achieved.

The designed lengths of the input region, the coupling region, the decoupling region, and the output region were 2000 μm, 1880 μm ($\sim L_c/2$), 2000 μm, and 6120 μm. According to the simulation results by R-soft, the coupling efficiencies of coupling and decoupling region were calculated as 97.4 % and 0.06 %. The sensitivity of the dual ARROW-based sensor can reach 475 a.u./RIU.

After all of the parameters of the dual ARROW-based sensor were designed, the devices were fabricated by using the equipments in the National Nano Device Laboratories. Then, the optical measurement system was set up at operating wavelength $\lambda = 0.6328$ μm. The sensitivity of the fabricated dual ARROW-based sensor was obtained as 1305 μm/RIU. The results show the feasibility of these types of sensors. However, the experimental results are much lower than simulation results. Possible reasons should be further investigated and the characteristics should be improved.

Bibliography

[1] R. C. Alferness, "Guided-wave devices for optical communication," *IEEE J. Quantum Electron.*, vol. 17, no. 6, pp. 946-959, June 1981.

[2] P. V. Lambeck, "Integrated opto-chemical sensors," *Sens. Actuators B*, vol. 8, pp. 103-116, 1992.

[3] B. J. Luff, R. D. Harris, J. S. Wilkinson, R. Wilson, and D. J. Schiffrin, "Integrated optical directional coupler biosensor," *Opt. Lett.*, vol. 21, no. 8, pp. 618-620, Apr. 1996.

[4] M. S. Hsu, "Design, Fabrication, and Characterization of Si-Based Dual ARROW Power Splitters," M. S. Thesis, National Chiao Tung University, Hsinchu, Taiwan, R. O. C., 2011.

[5] C. X. Sue, "Design, Fabrication, and Characterization of Si-Based Dual ARROW Power Splitters," M. S. Thesis, National Chiao Tung University, Hsinchu, Taiwan, R. O. C., 2010.

[6] M. A. Duguay, Y. Kokubun, T. L. Koch, and L. Pfeiffer, "Antiresonant reflecting optical waveguides in SiO_2-Si multilayer structures," *Appl. Phys. Lett.*, vol. 49, no. 1, pp. 13-15, Jan. 1986.

[7] N. Fabricius, G. Gauglitz, and J. Ingenhoff, "A gas sensor based on an integrated optical Mach-Zehnder interferometer," *Sens. Actuators B*, vol. 7, pp. 672-676, 1992.

[8] A. Brandenburg, R. Edelhauser, and F. Hutter, "Integrated optical gas sensors using organically modified silicates as sensitive films," *Sens Actuators B*, vol. 11, pp. 361-374, 1993.

[9] R. G. Heideman, R. P. H. Kooyman, and J. Greve, "Performance of a highly sensitive optical waveguide Mach-Zehnder interferomter immunosensor," *Sens. Actuators B*, vol. 10, pp. 209-217, 1993.

[10] G. H. Cross, A. Reeves, S. Brand, M. J. Swann, L. L. Peel, N. J. Freeman, and J. R. Lu, "The metrics of surface adsorbed small molecules on the Young's fringe dual-slab waveguide interferometer," *J. Phys. D*, vol. 37, no. 1, pp. 74-80, Jan. 2004.

[11] T. Tamir (Ed.), *Guided-Wave Optoelectronics*, Springer-Verlag, 1990.

[12] K. Okamoto, *Fundamentals of Optical Waveguides*, Academic Press, 2000.

[13] R. M. Knox and P. P. Toulios, "Integrated circuits for millimeter through optical frequency region," in *Proc. MRI Symp. Submillimeter Waves*, J. Fox, Ed., Brooklyn: Ploytechnic Press, pp. 497-516, 1970.

[14] H. Kogelnik, "Theory of optical waveguides," in *Guided-Wave Optoelectronics*, T. Tamir, Ed. Berlin, Germany: Springer-Verlag, 1990, ch. 2.

[15] K. S. Chiang, "Analysis of optical fibers by the effective-index method," *Appl. Opt.*, vol. 25, no. 3, pp. 348-354, Feb. 1986.

[16] T. Chung and N. Dagli, "An assessment of finite different beam propagation method," *IEEE J. Quantum Electron.*, vol. 26, no. 8, pp. 1335–1339, Aug. 1990.

[17] C. K. Chen, P. Berini, D. Feng, S. Tanev, and V. P. Tzolov, "Efficient and accurate numerical analysis of multilayer planar optical waveguides in lossy

anisotropic media," *IEEE Photion. Technol. Lett.*, vol. 7, no. 8, pp. 260-272, 2000.

[18] E. A. J. Marcatili, "Dielectric rectangular waveguide and directional coupler for integrated optics," *Bell Syst. Tech. J.*, vol. 48, no. 9, pp. 2071-2072, 1969.

[19] K. S. Chiang, "Dual effective-index method for the analysis of rectangular waveguides," *Appl. Opt.*, vol. 25, pp. 2169-2174, 1986.

[20] J. J. Deng, "Analysis and disign of antiresonant reflecting optical waveguides with discontinuities," Ph. D. dissertation, National Chiao Tung University, Hsinchu, Taiwan, R. O. C., Oct. 2000.

[21] W. P. Huang, A. Nathan, R. M. Shubair, and Y. L. Chow, "The modal characteristics of ARROW structures," *IEEE J. of Lightwave Technol.*, vol. 10, no. 8, pp. 1015-1022, 1992.

[22] J. J. Deng, "Analsis and design of antiresonant reflecting optical waveguide devices with discontinuities," Ph. D. Dissertation, National Chiao Tung University, Hsinchu, Taiwan, R.O.C., 2000.

[23] Y. H. Chen and Y. T. Huang, "Coupling-efficiency analysis and control of dual antiresonant reflecting optical waveguides," *IEEE J. Lightwave Technol.*, vol. 14, pp. 1507-1513, June 1996.

[24] Toshihiko Baba and Yasuo Kokubun, "Dispersion and Radiation Loss Characteristics of Antiresonant Reflecting Optical Waveguides Numerical Results and Analytical Expressions," *IEEE J. Quantum Electron.*, vol. 28, no. 7, jul. 1992.

[25] M. Mann, U. Trutschel, C. Wachter, L. Leine, and F. Lederer, "Directional coupler based on antiresonant reflecting optical waveguides," *Opt. Lett.*, vol. 16, no. 11, pp. 805-807, june 1991.

[26] H. F. Taylor and A. Yaiiv, "Guided wave optics," in *Proc. IEEE*, vol. 62, pp. 1044-1060, Aug. 1974.

[27] D. Marcuse, "The coupling of degenerate modes in two parallel dielectric waveguides," *Bell Syst. Tech. J.*, vol. 50, pp. 1791-1816, 1971.

[28] H. Kogelnik and R. V. Schmidt, "Switched directional couplers with alternating AB," *IEEE J. Quantum Electron.*, vol. QE-12, pp. 396-401, July 1976.

[29] A. Yariv, "Coupled mode theory for guided-wave optics," *IEEE J. Quantum Electron.*, vol. QE-9, pp. 919-933, Sep. 1973.

[30] D. M.arcuse, *Light Transmission Optics*, Van Nostrand, New York, 1972.

[31] A. Hardy and W. Streifer, "Coupled mode theory of parallel waveguides," *IEEE J. Lightwave Technol.*, vol. LT-3, pp. 1135-1146, Oct. 1985.

[32] Y. Suematsu and K. Kishino, "Coupling coefficient in strongly coupled dielectric waveguides," *Rado Science*, vol. 12, no. 4, pp. 587-592, July-Aug. 1977.

[33] T. Baba, Y. Kokubun, T. Sakaki, and K. Iga, "Loss reduction of an ARROW waveguide in shorter wavelength and its stack configuration," *J. Lightwave Technol.*, vol. 6, no. 9, pp. 1440-1445, Sep. 1988.

[34] A. R. Forouhi and I. Bloomer, "Optical dispersion relatiions for amorphous semiconductors and amorphous dielectrics," *Phys. Rev. B*, vol. 34, no. 15, pp. 7018-7026, Nov. 1986.

[35] Shih-Hsin Hsu and Yang-Tung Huang, "Design and analysis of Mach-Zehnder interferometer sensors based on dual strip antiresonant reflecting optical waveguide structures," *Opt. Lett.*, vol. 30, no. 21, pp. 2897 2899, Nov. 1, 2005.

[36] H. J. W. Hoekstra, G. J. M. Krijnen, and P. V. Lambeck, "On the accuracy of the finite difference method for applications in beam propagation techniques," *Opt. Commun.*, vol. 94, pp. 506-507, 1992.

[37] H. J. W. Hoekstra, G. J. M. Krijnen, and P. V. Lambeck, "New formulation of the beam propagation method based on the slowly varying envelop approximation," *Opt. Commun.*, vol. 97, pp. 301-303, 1993.

Vita

Cheng-Han Lee was born in Taichung, Taiwan on June 18, 1988. He received the B. S. degree in Physics from National Chung-Cheng University (CCU) in June 2010. He entered the Institute of Electronics, National Chiao Tung University (NCTU) in September 2010. His major studies are integrated optics and nanophotonics. He received the M. S. degree from NCTU in July 2011.